Numerical Investigation and Optimization of High Performance Plasmonic Refractive Index Sensors

by

Sabiha Sharmin (Student ID : 160021047)

Ehsanuzzaman Surid (Student ID : 160021107)

Tasnim Zaman Adry (Student ID : 160021157)

BACHELOR OF SCIENCE
IN
ELECTRICAL AND ELECTRONIC ENGINEERING

Department of Electrical and Electronic Engineering
Islamic University of Technology (IUT)
Board Bazar, Gazipur-1704, Bangladesh.
June, 2021.

CERTIFICATE OF APPROVAL

The thesis titled, *"Numerical Investigation and Optimization of High Performance Refractive Index Sensors"* has been found satisfactory as accepted as partial fulfillment of the requirement for the Degree BACHELOR OF SCIENCE IN ELECTRICAL AND ELECTRONIC ENGINEERING on June 4, 2021.

Approved by :

Dr. Rakibul Hasan Sagor (Supervisor)
Associate Professor,
Electrical and Electronic Engineering Department,
Islamic University of Technology (IUT), Gazipur.

Declaration of Authorship

We, declare this thesis titled, *"Numerical Investigation and Optimization of High Performance Refractive Index Sensors"* and the works presented in it are our own. We verify that :

- This work has been done for the partial fulfillment of the Bachelor of Science in Electrical and Electronic Engineering degree at Islamic University of Technology (IUT).

- Any part of this has not been submitted elsewhere for the award of any Degree or Diploma.

- We have always clearly attributed the sources when we have consulted the published work of others.
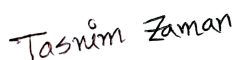
Submitted by :

—————————————

Sabiha Sharmin
Student ID : 160021047

—————————————

Ehsanuzzaman Surid
Student ID : 160021107

—————————————

Tasnim Zaman Adry
Student ID : 160021157

Table of Contents

List of Figures

List of Tables

List of Abbreviations

MIM	Metal-Insulator-Metal
ND	Nanodot
EM	Electromagnetic
FOM	Figure of Merit
FEM	Finite Element Method
LD	Lorentz-Drude
SRR	Square Ring Resonator
RI	Refractive Index
SPP	Surface Plasmon Polariton
CRR	Circular Ring Resonator
MUS	Material Under Sensing
Q-Factor	Quality Factor

Acknowledgment

"In the Name of Allah, the Most Beneficent, the Most Merciful. All the praises and thanks be to Allah, the Lord of the 'Alamin (mankind, jinns and all that exists)."

At the very begining, we would like to express our deepest gratitude to Almighty Allah (SWT) for giving us good health, strength and fortune needed to carry out this work.

We would like to extend our indebtedness appreciation to our thesis supervisor Dr. Rakibul Hasan Sagor, Associate professor, Department of Electrical and Electronic Engineering, Islamic University of Technology (IUT). His active guidance and willingness to share his vast knowledge helped us greatly to complete this work.

Our sincere thanks goes to Md.Farhad Hassan, Lecturer, Department of Electrical and Electronic Engineering, Islamic University of Technology (IUT), who helped us immensely to carry out this study as flawless as possible. We appreciate his attentive guidance, endless patience and encouragement throughout this study despite having a busy schedule.

We would also like to take the opportunity to thank all the faculty member of the Department of Electrical and Electronic Engineering at Islamic University of Technology (IUT) for their support and inspiration.

And finally, we are deeply appreciative of our parents, families and friends for their constant love and support.

Abstract

Plasmonic sensors based on *SPP* are replacing traditional bulky sensors in biosensing and chemical sensing applications, food adulteration, medical diagnostics owing to the distinctive optical properties of *MIM* models. Two sensor topologies based on metal-insulator-metal (*MIM*) waveguide are proposed in this work to meet the requirements of label-free detection, low cost, and quick response of a lab-on-chip biosensor. Using the finite element method (*FEM*) with scattering boundary condition, the transmission spectrum and E-field distributions are computed. The sensing performance in both structures is improved by inserting nanodots (NDs) in the high E-field region of the *MIM* structures. A *MIM* waveguide and a laterally coupled square ring resonator (SRR) with diagonally inserted NDs on two opposite sides of the square and a rectangular cavity offers a maximum sensitivity of 1550 nm/RIU and a maximum *FOM* of 68.45 initially. The second structure designed with a square ring resonator (SRR) and a circular ring resonator (CRR) provides an initial sensitivity of 2090 nm/RIU and the initial *FOM* is 41.6. Enforcing simultaneous optimization of structural parameters and strengthening light-matter interaction by filling NDs in high E-field region, the sensitivity of the first structure increases to 2470 nm/RIU with a *FOM* of 85.17. Similarly, a maximum sensitivity of 2850 nm/RIU with 105.95 *FOM* is recorded after the optimization of the second structure. The first proposed structure is investigated as a food adulterant detector, whereas the other is tested for its tolerance of possible manufacturing defect. The designs are comparable to many excellent sensors in the literature due to simplicity, compact design, and easy manufacturing process, as well as the plasmonic devices' desirable performance metrics.

Chapter 1

Introduction and Background

1.1   Surface Plasmon Polariton

The advancement of integrated electronic circuits has resulted in extraordinary data processing and transport capabilities and has had a significant impact on our lives over the last few decades. Signal delay and thermal problems associated with electronic interconnections preclude dramatic improvements in processor speed as the size of state-of-the-art transistors shrinks to the order of 50 nm or less [9]. Metal nanostructures can have the ideal combination of electronic and optical properties to address the above issues and realize the hope of dramatically faster processing speeds. Nanoplasmonics uses the specific optical properties of metallic nanostructures to allow routing and manipulation of light at the nanoscale. The ability of such devices to retain optical energy localized on the nanoscale due to modes known as surface plasmons (*SPs*) is a remarkable feature. Combined with current nanofabrication technologies that allow for the preparation of various standard patterns of particles, holes, or nanogratings, this technology allows for the development of effective, fast, and sensitive integrated multiplexed sensor systems for biological, chemical, and medical research [10, 11].
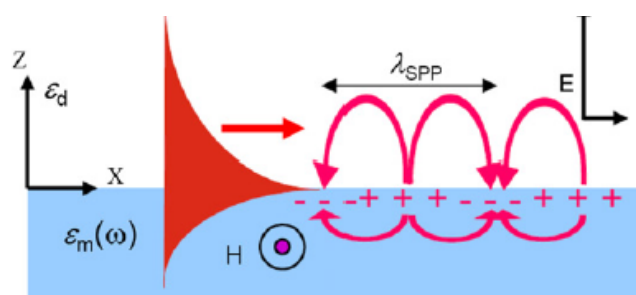
Figure 1.1: *SPP* propagation at the metal-dielectric interface [1].

Surface Plasmon Polaritons (*SPPs*) properties have recently been extensively studied for its use in the field of nano-sensors [12]. Surface plasmon polaritons (*SPPs*), also known as surface plasmons (*SPs*), are electromagnetic excitations that are coupled

to surface collective oscillations of free electrons in a substance, resulting in two-dimensional bound waves that propagate through metal-dielectric interfaces and decay exponentially into neighboring material [13]. They have the unparalleled potential to restrict the optical mode in the sub-wavelength scale. Because of the confinement, the electromagnetic field at the interface is enhanced, giving *SPPs* a high sensitivity to surface conditions. *SPPs* can exceed the diffraction limit and confine light in subwavelength dimensions, allowing nanoscale plasmonic devices to be developed [12, 14]. *SPPs* are the fundamental building blocks of plasmonics, a technology that can be used in fully integrated optical instruments [15]. In figure 1.1, the *SPP* propagation on the metal-dielectric interface is depicted.

1.2 Metal-Insulator-Metal Waveguide Topology

As the *SPPs* connected with individual metal-dielectric interfaces start communicating with each other in multiple-interface structures, several different SPP modes emerge [16, 17]. When the *SPP* modes aligned with two metal-dielectric interfaces are considered, it is discovered that the *SPP* modes can be aided by either a thin metal film abutting dielectrics or a thin dielectric layer surrounded by metals, which are referred to as the insulator-metal-insulator (*IMI*) or metal-insulator-metal (*MIM*) systems, respectively [18]. The nanostructure based on *IMI* has a long propagation range. As a consequence, the *IMI* structure is often known as a long-range surface plasmon (LRSP) [19, 20]. Metal-Insulator-Metal (*MIM*) structured waveguide is one of the many potential architectures for realizing *SPP* propagated plasmonic applications. With minimal propagation loss, a *MIM* waveguide can confine light to the subwavelength scale. This paves the way for the interconnection of fully integrated electronic circuits with optical circuits on the same chip, where electrons and photons serve as information carriers. The *MIM* setup offers nanoscale plasmonic gadgets like sensors [21, 22], color filters [23], demultiplexers [24, 25], diodes [26], Mach-Zehnder interferometers [27] etc.

1.3 Plasmonic Refractive Index Sensor

The refractive index sensor is one of the most important devices among plasmonic devices for its use to detect the refractive indices of various dielectric materials present in the configuration of the sensor. *MIM* waveguide-based plasmonic refractive index sensors are particularly sensitive to structural parameters and environmental media due to intense light-matter interaction near the metal-dielectric interface. As a result, using these sensors to track some unknown substance opens up new possibilities in nanoscale sensing. *MIM* waveguides have higher propagation loss than silicon photonic waveg-

uides, but they have better field containment [28]. The plasmonic refractive index sensor monitors the change in resonant wavelength to determine the refractive index of the unknown material. *SPPs* in a *MIM* configuration are good candidates for compact integrated optical circuits, and they can also be used for on-chip applications. Among the numerous applications of plasmonic *MIM*-based RI sensors, detecting food adulterants is a promising area of sensing. The consistency of various food and chemical products can be assured by quantifying their refractive indices [29]. The detection of adulterants in pure honey is used as an example of detecting food adulterations. In this thesis, two unique refractive index sensor designs with increased sensitivity and *FOM* will be proposed. One of the proposed designs will be presented for detecting adulterants in pure honey (refractive index 1.351 to 1.353). The sensors could be used to build bio-implantable lab-on-a-chip applications.

1.4   Literature Review

Plasmonic sensors have been researched and developed since the 1980s. Various plasmonic sensors have been developed over the years by utilizing the supreme features of *SPP*. Because of its deep subwavelength EM wave localization, ease of fabrication, label-free detection, and low time response, *MIM*-based refractive index sensors have gained considerable attention in lab-on-chip bio-sensing [30]. Nanosensors with *MIM* configuration have comparatively low sensitivity than conventional fiber optic sensors. To overcome this hurdle, researchers are more concerned with increasing the sensitivity of *MIM* sensors while leaving other performance metrics unaffected. Over the years, efforts have been made to improve the sensitivity using *MIM* waveguide with numerous structures [4, 22].

In 2015, Xie et al. proposed a *MIM*-based plasmonic refractive index sensor with a side-coupled hexagonal cavity (figure 1.2a) that provides a maximum sensitivity of 1562 nm/RIU [2]. A maximum sensitivity of 985 nm/RIU was recorded by Chen et al. in 2016 by coupling a slot resonator with *MIM* waveguide [3]. Rakhsani et al. presented an *SPP* sensor with a sensitivity value as high as 2320 nm/RIU [4]. Coupling the *MIM* waveguide with two stubs and a ring resonator, Zhang et al. presented a refractive index sensor with a maximum sensitivity of 1268 nm for every refractive index unit [5]. Placing a pentagonal ring-resonator with a straight waveguide as shown in figure 1.2e, Al mahmud et al. reported a maximum sensitivity of 1790.3 nm/RIU [6]. Recently, Butt et al. have designed a refractive index sensor based on a bow-tie configuration that exhibit a maximum sensitivity of 2300 nm/RIU [7]. The comparison of

performance parameters of recently reported *MIM* waveguide based refractive index sensor is listed in Table 1.1.

(a)   **(b)**

(c)   **(d)**

(e)   **(f)**
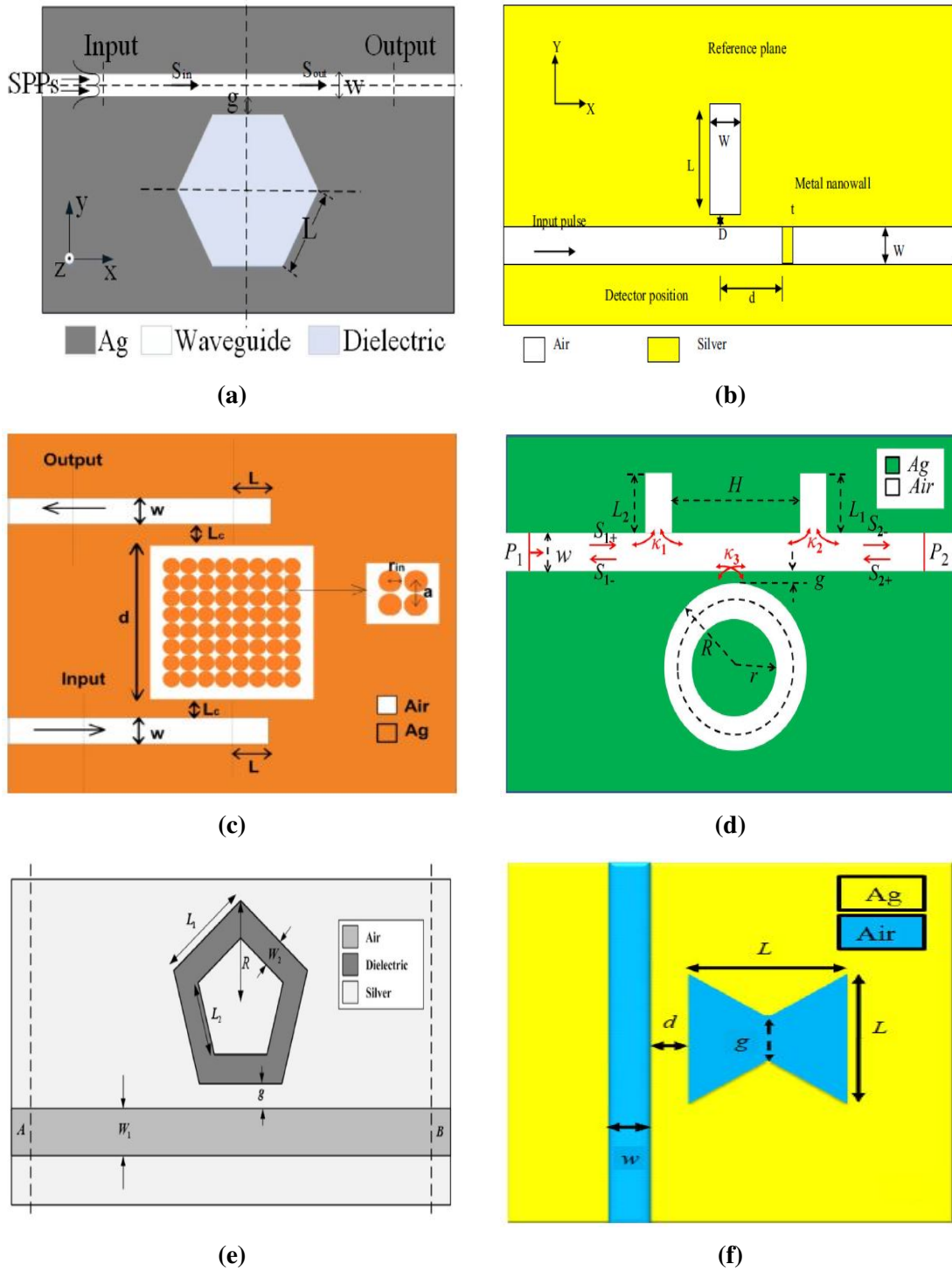
Figure 1.2: RI sensors based on plasmonic *MIM* waveguide that have recently been developed by (a) Xie et al. [2], (b)Chen et al. [3], (c) Rakhsani et al. [4], (d) Zhang et al. [5], (e) Al mahmud et al. [6], and (f) Butt et al. [7].

Table 1.1: Comparison of sensitivity (*S*) and figure of merit (*FOM*) of different sensors reported in this work.

Ref.	Sensor Design	Metal Model	Sensitivity (nm/RIU)	FOM	Year
[31]	Loop-stub	Drude	1132	31.44	2013
[2]	Side-coupled hexagonal cavity	Lorentz-Drude	1562.5	88.6	2015
[3]	Slot resonator	Lorentz	985	28.2	2016
[4]	Nanorods in square array and two waveguides	Lorentz-Drude	2320	-	2017
[32]	Rectangular and ring resonator	Debye-Drude	1125	75	2017
[33]	Multi channel split ring resonator	Drude	1217	24.34	2018
[34]	Square ring resonator	Lorentz-Drude	1200	19.7	2019
[28]	Nano square ring resonator	Lorentz-Drude	1320	16.7	2019
[35]	*MIM* waveguide coupled by a square ring resonator	Lorentz-Drude	1367	27.6	2019
[36]	Nanodots loaded square ring resonator	Debye-Drude	1240	20	2019
[37]	Nano-wall square split ring resonator	Lorentz-Drude	793.3	52.9	2019
[5]	Two stubs and a ring resonator	Debye-Drude	1268	280	2019
[38]	Double square cavities	Lorentz-Drude	1380	102	2020
[39]	Square ring resonators with nanodots	Lorentz-Drude	907	40.8	2020
[6]	Ring-type pentagonal resonator	Lorentz-Drude	1790.3	45.6	2020
[40]	Double rectangular cavity	Drude	1228.67	-	2020
[7]	Bow-Tie Cavity	Lorentz-Drude	2300	31.5	2020
[30]	Concentric Double ring resonator	Drude	1070	-	2020

(Continued...)

Ref.	Sensor Design	Metal Model	Sensitivity (nm/RIU)	FOM	Year
[8]	Two rectangular stubs and an elliptical ring resonator	Drude	1550	43.05	2020
[22]	Three parallel rectangular cavity	Drude	1556	14.83	2020

The main objective of such design variation as summarized in table 1.1 is to improve the device's sensitivity to detect a minimal difference in the ambient refractive index. Plasmonic sensors are widely used in variety of areas including healthcare industry, biotechnology, pharmaceutical industry, food and environment monitoring.

1.5 Thesis Objective

The objectives of this thesis are as follows:

- To develop a highly sensitive refractive index sensor with *MIM* configuration.

- To numerically investigate the sensitivity and *FOM* of the optimized sensor.

- To analyze the manufacturing process and tolerance limit of the proposed structure.

- To examine the food adulteration detection capability of the sensor.

1.6 Thesis Outline

- Chapter 1 addresses the fundamentals of *SPPs*, including the *MIM* waveguide and the numerous plasmonic sensors, such as the refractive index sensor. The new advances in plasmonic metal-insulator-metal waveguide-based refractive index sensors are also addressed, and the thesis outline has been described.

- Chapter 2 discusses the fundamental wave equations and material simulation of metals. Maxwell's equation and generic constitutive connections are also discussed to realize Maxwell's equation with various media. This chapter also covers the Drude, Lorentz, and Lorentz-Drude models for modeling the permittivity of a substance with frequency. The topic discusses the specifics of *FEM*, such as how to calculate S-parameters and transmittance theoretically.

- Chapter 3 includes theoretical investigation of ring resonator with *MIM* configuration. This chapter also presents the discussion of basic performance metrics for evaluating RI sensor, and re-simulation of an already published work.

- Chapter 4 demonstrates two unique *MIM* refractive index sensor designs. Details of the initial structural design, fabrication, tolerance, and performance of the proposed sensors are also presented. The proposed sensors are subjected to sequential optimization, and performance metrics after the optimization are also recorded. One of the proposed structure is demonstrated as a food adulterant detector with adulterated honey as sensing media.

- Chapter 5 determines the best structural parameters in terms of sensitivity and *FOM* of the refractive index sensors in the literature. Plans for possible improvement are also explored.

Chapter 2

Wave Theory and Material Modeling

2.1 Electromagnetic Wave Theory

In order for *SPPs* to propagate along the metal-insulator interface, there needs to be a relation that describes the production of the magnetic and electric fields. *Maxwell's* equation is the main principle that can be used to derive the wave equation that governs the propagation of the EM wave in different media. Transmittance is a key indicator of the plasmonic sensor performance which indicates the relationship between input and output of the device. Finite element method (*FEM*) is one of the numerical tools to evaluate the electromagnetic field of the plasmonic device.

2.1.1 Maxwell's Equation

Fundamental Laws

The relationship that describe the fundamental electromagnetic quantity is explained by *Maxwell's* equations. The equations can be expressed in differential or integral forms which is the basis for electromagnetic analysis. The Finite Element Method (*FEM*) uses the differential form of *Maxwell's* equations and are expressed in the time-varying fields as,

$$Ampere - Maxwell\ Law: \quad \nabla \times H = J + \frac{\partial D}{\partial x} , \quad (2.1)$$

$$Faraday's\ Law: \quad \nabla \times E = -\frac{\partial B}{\partial t} , \quad (2.2)$$

$$Gauss'\ Law: \quad \nabla.D = \rho , \quad (2.3)$$

$$Gauss'\ Law\ for\ magnetism: \quad \nabla.B = 0 . \quad (2.4)$$

The symbols *H,D,E,B,J*, and ρ denotes magnetic field intensity, electric flux density, electric filed intensity, magnetic flux density, electric current density, and volume charge density, respectively. The law of charge conservation connects the volume charge density and current density. This continuity equation is expressed as,

$$\nabla . J = -\frac{\partial P}{\partial t} \; . \tag{2.5}$$

2.1.2 Constitutive Relations

To understand the generation of charge and current, the constitutive equations play an important role that explains the nature of the material in contact with the fields. These equations are given as,

$$D = \epsilon_0 E + P \; , \tag{2.6}$$

$$B = \mu_0 (H + M) \; , \tag{2.7}$$

$$J = \sigma E \; , \tag{2.8}$$

where, ϵ_0 denotes the electric permittivity of vacuum, μ_0 is the magnetic permeability of vacuum, and σ represents the electric conductivity.

The constitutive equation for linear materials which have constant material properties with the variation of applied field is given by,

$$B = \mu_0 (1 + \chi_m) H = \mu_0 \mu_r H = \mu H \; , \tag{2.9}$$

$$D = \varepsilon_0 (1 + \chi_e) E = \varepsilon_0 \varepsilon_r E = \varepsilon E \; , \tag{2.10}$$

here,

$$\varepsilon_r = (1 + \chi_e) \; ,$$

$$\mu_r = (1 + \chi_m) \; .$$

2.1.3 Wave Equation

The propagation of the EM waves is governed by the wave equation. This can be derived from equation 2.2 with ∇, which gives us,

$$\nabla \times (\nabla \times E) = \nabla \times (-\frac{\partial B}{\partial t}) = -\frac{\partial}{\partial t}(\nabla \times B) \ . \qquad (2.11)$$

From equation 2.1, 2.9, and 2.10 we get,

$$\nabla \times (\nabla \times E) = -\mu\varepsilon\frac{\partial^2 E}{\partial t^2} \ . \qquad (2.12)$$

If $\frac{\partial}{\partial t} = j\omega$, $\varepsilon = \varepsilon_0\varepsilon_r$, and $\mu = \mu_0\mu_r$ is taken into consideration, the equation transforms to,

$$\nabla \times (\mu_r^{-1}\nabla \times E) - k_0^2\varepsilon_r E = 0 \ , \qquad (2.13)$$

where, k_0 is the wave number and expressed as,

$$k_0 = \omega\sqrt{\mu_0\varepsilon_0} = \frac{\omega}{c_0} \ . \qquad (2.14)$$

Equation 2.13 can be redesigned by using the relation between refractive index n and ε_r, $\varepsilon_r = n^2$. Assuming $\mu_r = 1$, the equation becomes,

$$\nabla \times (\nabla \times E) - k_0^2 n^2 E = 0 \ . \qquad (2.15)$$

2.2 Plasmonic Material Modeling

Metals are perfect conductors at low frequencies or for long wavelengths. As they have zero field, they do not possess any dispersive nature. However, at optical frequencies metals exhibit dispersive nature. At frequency higher than optical range, metals behave as dielectrics.

The behavior of material under the presence of an external oscillating electromagnetic filed can be determined by three vectors. They are E (electric field intensity), P (polarization density), and D (electrical flux density). They are given as,

$$D(\omega) = \varepsilon(\omega)E(\omega) \ , \tag{2.16}$$

$$P(\omega) = \varepsilon_0\chi(\omega)E(\omega) \ , \tag{2.17}$$

$$D(\omega) = \varepsilon_0E(\omega) + P(\omega) \ , \tag{2.18}$$

Combining equations 2.17 and 2.18 we get

$$D(\omega) = \varepsilon_0E(\omega)(1 + \chi(\omega)) \ . \tag{2.19}$$

here, χ is the electric susceptibility. The susceptibility is a measure of how easily a material is polarized in response to an applied electric field, and it is a dimensionless quantity.

Now, comparing equation 2.16 and 2.19, the relation between permittivity and susceptibility stands as,

$$\varepsilon(\omega) = \varepsilon_0(1 + \chi(\omega)) \ , \tag{2.20}$$

Therefore, the relative permittivity is given by,

$$\varepsilon_r(\omega) = 1 + \chi(\omega) \ . \tag{2.21}$$

Although the above values become simple for linear isotropic materials such as glass, in case of a dispersive material, the frequency dependent permittivity and susceptibility should be modeled precisely, to obtain the perfect response of the material for certain electromagnetic excitation. The Drude model, Lorentz model and Lorentz-Drude model are widely used to address this dependency mathmetically.

2.2.1 The Drude model

Paul Drude developed the Drude model of electrical conduction. The model described the metal as a volume filled with positive ions, surrounded by the gas of electrons which follows the kinetic theory of gases. The electrons are free to move inside the

metal without other electrons affecting any of them. The electrons experience two forces,

- Driving force F_d ,

- Damping force F_g .

These two forces, the driving force and the damping force and are expressed as,

$$F_d = qE = -eE \; , \tag{2.22}$$

$$F_g = -\Gamma v \; . \tag{2.23}$$

These two forces have opposite directions and the resultant force will be,

$$F = F_d - F_g. \tag{2.24}$$

According to *Newton's* first law of motion we can write,

$$mr^{''} = -eE + \Gamma r^{'} \; . \tag{2.25}$$

where,
$m =$ the mass of electron,
$\Gamma =$ damping constant,
$r =$ the displacement in meter,
$v =$ electron's velocity, and
$q =$ charge of electrons. Here, the prime repesents differentiation order with respect to time.

The equation for the time harmonic electric field and time harmonic displacement is given as,

$$E(t) = E_0 e^{-j\omega t} \Leftrightarrow E(\omega) \; , \tag{2.26}$$

$$r(t) = R_0 e^{-j\omega t} \Leftrightarrow R(\omega) \; . \tag{2.27}$$

The frequency domain representation of equation 2.25 is,

$$mR''(\omega) - \Gamma mR'(\omega) + eE(w) = 0. \tag{2.28}$$

The derivatives of frequency domain will give,

$$-m\omega^2 R''(\omega) + j\omega\Gamma mR'(\omega) + eE(\omega) = 0 . \tag{2.29}$$

Simplifying equation 2.25,

$$R(\omega) = \frac{-e}{m(j\Gamma\omega - \omega^2)}E(\omega) . \tag{2.30}$$

The polarization for n number of electrons is given by,

$$P(\omega) = -neR(\omega) , \tag{2.31}$$

or,

$$P(\omega) = \frac{e^2 n}{m(j\Gamma\omega - \omega^2)}E(\omega) . \tag{2.32}$$

The susceptibility obtained from the above equation is expressed as,

$$\frac{P(\omega)}{\varepsilon_0 E(\omega)} = \frac{e^2 n}{\varepsilon_0 m(j\Gamma\omega - \omega^2)} = \chi(\omega) . \tag{2.33}$$

Placing this value in equation 2.10,

$$\varepsilon_r(\omega) = 1 + \frac{e^2 n}{\varepsilon_0 m(j\Gamma\omega - \omega^2)} . \tag{2.34}$$

If we take ω_p as the plasma frequency that will give us,

$$\omega_p^2 = \frac{e^2 n}{\varepsilon_0 m} . \tag{2.35}$$

Giving the frequency dependent flux density to be,

$$D(\omega) = \varepsilon_0 (1 + \frac{\omega_p^2}{j\Gamma\omega - \omega^2})E(\omega) . \tag{2.36}$$

13

At low frequency, $\Gamma\omega \ll 1$, which reduces the dispersive relation to,

$$D(\omega) = \varepsilon_0(1 - \frac{\omega_p^2}{\omega^2})E(\omega) \ . \tag{2.37}$$

2.2.2 The Lorentz Model

Figure 2.1 shows that the Lorentz model paints a much simpler picture of the atom. This model is very useful to visualize the atom-field interaction. This model explains the connection between the smaller mass electron and larger mass nucleus where the electrons do not move freely rather are bound to atoms. Hence, a restoring force, F_r acts between them that is expressed as F_r.

$$F_r = -kr \ , \tag{2.38}$$

here, k represents the spring constant in Newtons per meter.
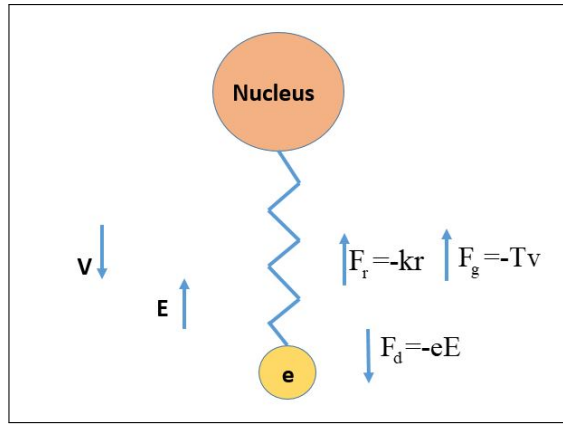
Figure 2.1: Lorentz Model

Similarly, according to the law of motion,

$$mr'' + \Gamma mr'(\omega) + mkr + eE = 0 \ . \tag{2.39}$$

Equation 2.39 is represented in frequency domain as,

$$R(\omega)(m\omega_0^2 + j\omega\Gamma m - m\omega^2 - eE(\omega)) = 0 \ . \tag{2.40}$$

14

If the natural frequency is $\omega_0 = \sqrt{\frac{k}{m}}$ then,

$$R(\omega) = \frac{-e}{m(\omega_1^2 + j\omega\Gamma - \omega^2)}E(\omega) \ . \tag{2.41}$$

The susceptibility can therefore be given as,

$$\frac{P(\omega)}{\varepsilon_0 E(\omega)} = \frac{e^2 n}{\varepsilon_0 m(\omega_0^2 + j\omega\Gamma - \omega^2)} = \chi(\omega) \ . \tag{2.42}$$

So, from the equation 2.19 the expression for D in frequency domain is given by,

$$D(\omega) = \varepsilon_0(1 + \frac{\omega_p^2}{\omega_0 + j\omega\Gamma - \omega^2})E(\omega) \ . \tag{2.43}$$

2.2.3 The Lorentz-Drude Model

The Lorentz-Drude model represents the most general form of EM field incident on metal. This model specifies two different types of electrons oscillating inside the metal, and as they oscillate they contribute to the overall permittivity of the metal. The Drude model is best suited for free electrons, while the Lorentz model is particularly fit for bound electrons. The permittivity therefore of the Lorentz-Drude model is,

$$\varepsilon = \varepsilon_{free} + \varepsilon_{bound} \ , \tag{2.44}$$

where,
$\varepsilon_{free} = 1 + \frac{\omega_p}{j\Gamma\omega - \omega^2}$,
$\varepsilon_{bound} = \frac{\omega_p}{\omega_0 + j\omega\Gamma - \omega^2}$.

Therefore, combining both the model, frequency domain representation of the electric field desity D is,

$$D(\omega) = x_0(1 + \frac{\omega_p}{j\Gamma\omega - \omega^2} + \frac{\omega_p^2}{\omega_0 + j\omega\Gamma - \omega^2}) \ . \tag{2.45}$$

Equation 2.45 is known as the Lorentz-Drude model.

15

2.3 Simulation Modeling

2.3.1 *FEM* for Electromagnetic Field Calculation

The finite element method (*FEM*) can solve problems of complex geometry and in-homogeneous media more effectively than other conceptually simpler and easier to code mathematical methods such as the finite difference method, method of moments (MOM), and so on.

Electromagnetic fiels are calculated with *Maxwell's* equation. The electrical voltage V, and the magnetic potential vector A are expressed as,

$$B = \nabla \times A \,, \tag{2.46}$$

$$E = -\nabla \times V \,. \tag{2.47}$$

Considering equation 2.46, equation 2.2 can be transferred into,

$$\nabla \times E = -\nabla \times \left(\frac{\partial A}{\partial t}\right) \,. \tag{2.48}$$

As the electric field potential for the non-static fields is increased with an induced voltage,

$$E = -\nabla V - \left(\frac{\partial A}{\partial t}\right) \,. \tag{2.49}$$

Conductors replace the term charge density with Dirichlet type boundary equation. The potential equation reduces to a *Laplace* equation,

$$\nabla.(\varepsilon \nabla V) = 0 \,, \tag{2.50}$$

here, ε denotes a diagonal tensor, neglecting the off-diagonal coupling terms:

$$\varepsilon = \begin{bmatrix} \varepsilon_x & 0 & 0 \\ 0 & \varepsilon_y & 0 \\ 0 & 0 & \varepsilon_z \end{bmatrix} \,. \tag{2.51}$$

The electric field energy is expressed as,

$$W_E = \int_V \frac{D.E}{2} dV = \int_V \frac{\varepsilon |E|^2}{2} dV \ . \tag{2.52}$$

Scattering parameters can be evaluated using the equation,

$$S_{ij} = \frac{\int_{porti}(E_j.E_i^*)dA_i}{\int_{porti}(E_j.E_j^*)dA_i} \ . \tag{2.53}$$

The time average reflection and transmittance coefficient, T is obtained by,

$$T = |S_{ij}|^2 \ . \tag{2.54}$$

2.3.2 Scattering Boundary Condition (*SBC*)

A transparent boundary condition for incoming and outgoing (scattered) incident waves, is obtained by applying scattering boundary condition (*SBC*) at the simulation window. The simulation window is perfectly transparent for outgoing (scattered) wave, which is defined as,

$$E = E_{SC}e^{-jk(n.r)} + E_0 E^{-jk(K.r)} \ , \tag{2.55}$$

where, E_0 represents the incident plane wave propagating along the k direction. The boundary condition is perfectly transparent for the perpendicular scattered plane wave and partially transparent for the oblique incident plane wave (scattered).

Chapter 3

Parameters for an RI Sensor's Quality

Theoretical investigation of ring resonator based structure will clarify the obtained simulation results including resonant wavelength, transmission mode. The performance metrics (e.g. *sensitivity*, *FOM*, *Q-factor*) evaluates sensing capacity of the design. Any already published work can be used to validate the simulation configuration, by re-simulating it. Moreover, a comparison between numerical results of the re-simulated work and the original work will ensure precision of the process.

3.1   Ring Resonator

The basic structure of a ring resonator based *MIM* waveguide is presented in figure 3.1. The relation between input and output is defined by,

$$\begin{bmatrix} E_{t1} \\ E_{t2} \end{bmatrix} = \begin{bmatrix} t & k \\ -k^* & t^* \end{bmatrix} \begin{bmatrix} E_{i1} \\ E_{i2} \end{bmatrix} . \tag{3.1}$$

Where,

k and t = coupling parameters,

E_{i1} = the source complex mode amplitude at the input port,

E_{t1} = the transmission complex mode amplitude at the output port,

E_{t2} = coupled complex mode amplitude to the cavity,

E_{i2} = complex mode amplitude transmitted from the cavity.

Since the networks are reciprocal, the matrix appears symmetric,

$$\left| k^2 \right| + \left| t^2 \right| = 1 . \tag{3.2}$$

Considering E_{i1}=1 for simplification,

$$E_{i2} = \alpha.e^{j\theta} E_{t2} , \tag{3.3}$$

18
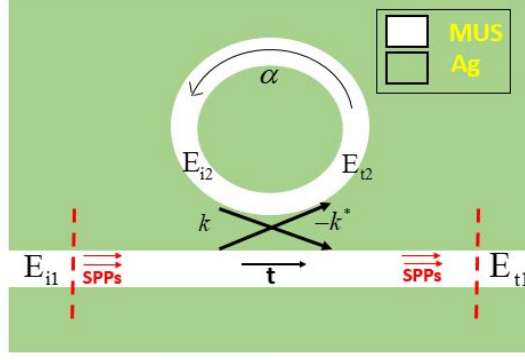
Figure 3.1: Plasmonic waveguide coupled with ring resonator.

where, α is the coefficient loss of the ring and θ is expressed as,

$$\theta = \frac{\omega L}{c} = \frac{2\pi c_0 L}{\lambda_c} = k.n_{eff}.L = \beta.L \, , \tag{3.4}$$

here, c is the phase velocity of the ring resonator which equals to $\frac{c_0}{neff}$, n_{eff} indicates the effective refractive index, and L is the effective propagation length of the coupled wave.

Equation 3.1 and 3.3 can be re-written as,

$$E_{t2} = -k^* + t^*(\alpha e^{j\theta} E_{t2}) \, ,$$

$$E_{t2}(1 - \alpha e^{j\theta}) = -k^* \, ,$$

$$E_{t2} = \frac{-k^*}{1 - \alpha e^{j\theta}} \, , \tag{3.5}$$

$$E_{t1} = \frac{-\alpha + te^{-j\theta}}{-t^*\alpha t^* + e^{-j\theta}} \, , \tag{3.6}$$

$$E_{i2} = \frac{-\alpha k^*}{-\alpha t^* + e^{-j\theta}} \, . \tag{3.7}$$

Having $\theta + \varphi_t = 2\pi m$ on resonance, the transmission power of the waveguide P_{t1} and the circulating power inside the ring P_{i2} can be expressed as,

$$P_{t1} = |E|_{t1} = \frac{\alpha^2 + |t|^2 - 2\alpha |t| \cos(\theta + \varphi)}{1 + \alpha^2 |t|^2 - 2\alpha |t| \cos(\theta + \varphi)} = \frac{(\alpha - |t|)^2}{(1 - \alpha |t|)^2} \, , \tag{3.8}$$

$$P_{i2} = |E|_{i2} = \frac{\alpha^2(1 - |t|^2)}{(1 - \alpha |t|)^2} \, , \tag{3.9}$$

where, $t = |t| \, e^{j \varphi t}$ is the coupling loss, φ_t represents the coupling phase and m is an integer.

Resonant wavelength λ_m can be derived from equation 3.4,

$$\frac{2\pi}{\lambda_m} . n_{eff} . L = 2\pi (m - \frac{\varphi_t}{2\pi}) \; , \tag{3.10}$$

$$\lambda_m = \frac{n_{eff} . L}{m - \left(\frac{\varphi_t}{2\pi}\right)} \; . \tag{3.11}$$

Halogen lamp technology, with its wide light spectrum encompassing the entire wavelength range in which λ_{res} is supposed to exist, is ideal for injecting light into the waveguide. w denotes width of the *MIM* waveguide, and is kept $w << \lambda_{incident}$ to establish fundamental TM_0 mode propagation. Dispersion equation of this mode can be expressed as,

$$\tanh(\frac{k_{MUS} * w}{2}) = -\frac{\varepsilon_{MUS} * k_{Silver}}{\varepsilon_{silver} * k_{MUS}} \; ,$$

$$k_{MUS,Silver} = \sqrt{\beta_{SPP}^2 - \varepsilon_{MUS,Silver} * k_0^2} \; ,$$

$$n_{eff} = \frac{\beta_{SPP}}{k_0} = \frac{2\pi}{\lambda} \; , \tag{3.12}$$

here,
$\varepsilon_{MUS} = n_{MUS}^2$ = dielectric constant of MUS,
ε_{Silver} = dielectric constant of silver,
n_{eff} = effective refractive index,
β_{SPP} = propagation constant, and
k_0 = free space wavenymber.

3.2 Parameters of Sensor Quality

The challenge for researchers is to enhance sensor performance by designing better waveguide configurations. Sensitivity, figure of merit (*FOM*), and quality factor (*Q-factor*) are considered to be the determinants of plasmonic RI sensor's performance.

3.2.1 Sensitivity (*S*)

Different types of structures like double cavity, ring resonators are designed to obtain spectral response which has Lorentzian peak and Fano type resonance. For the sensor to be able to detect the refractive index, the material whose refractive index is to be measured is placed in the cavity. The resonant wavelength exhibits redshift or blueshift if there is any refractive index change. Sensitivity (*S*), the most significant characteristic of an RI sensor is measured by the shift in resonance wavelength ($\Delta\lambda$) over the change in refractive index (Δn). The equation is expressed as follows [41],

$$S = \frac{\Delta\lambda}{\Delta n} \ . \tag{3.13}$$

Where, $\Delta n = n2 - n1$ change in refractive index, and $\Delta\lambda$ is the shift of resonant wavelength, as depicted in figure 3.2. The transmittance dip shift can be determined using a modern spectrometer, and hence the sensitivity of an RI sensor can be easily calculated.

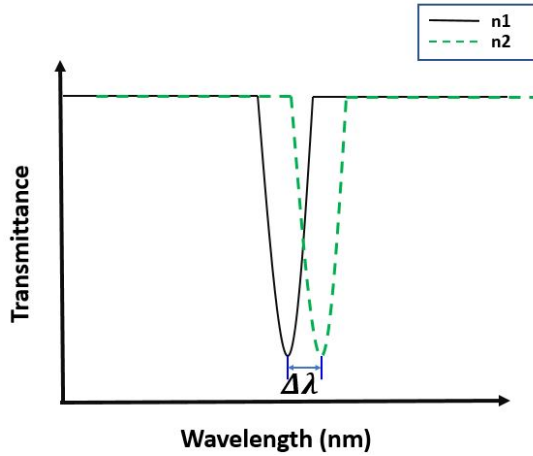**Figure 3.2:** Transmittance vs. wavelength for sensitivity calculation.

3.2.2 Figure of Merit (*FOM*)

FOM is typically used in sensing applications to test sensing efficiency further and is expressed as,

$$FOM = \frac{S}{FWHM} \ . \tag{3.14}$$

In equation 3.14, *S* represents sensitivity, and *FWHM* is abbreviated from Full Width at Half Maximum and defined as,

$$FWHM = \lambda_2 - \lambda_1 \ , \tag{3.15}$$

where, λ_1 and λ_2 are the wavelength values at $\frac{T_{max}-T_{min}}{2}$ as shown in figure 3.3.
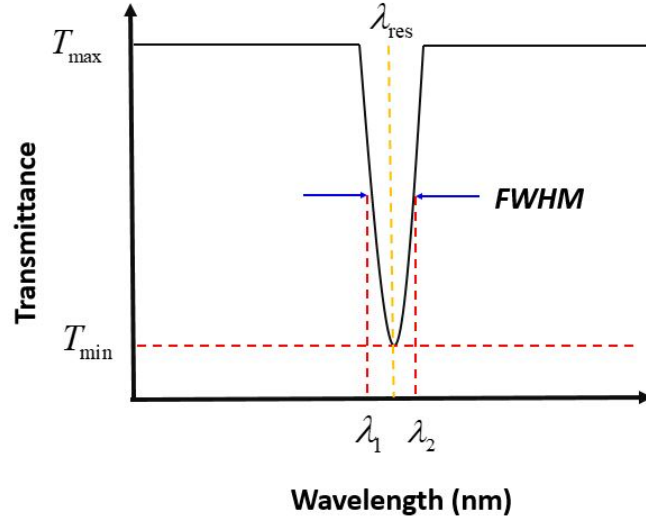
Figure 3.3: Transmittance profile for evaluation of *FOM*.

3.2.3 Quality Factor (*Q-factor*)

Sensors with high *Q-factor* are suitable for a wide range of application including narrow-bandwidth filters, high-performance lasers, high-efficiency nonlinear optical devices, and high-sensitivity sensors. The expression for *Q-factor* is given by,

$$Q - factor = \frac{\lambda_{res}}{FWHM} \, . \tag{3.16}$$

Where, λ_{res} is the resonance wavelength, as shown in figure 3.3. *Q-factor* determines filtering performance of the device.

3.3 Simulation Result validation with COMSOL Multiphysics

The simulation set-up using COMSOL Multiphysics needs to be validated before proceeding with numerical investigation of the proposed sensor. Therefore, a plasmonic refractive index sensor proposed by Su et al. [8], titled *"Sensing Features of the Fano Resonance in an MIM Waveguide Coupled with an Elliptical Ring Resonant Cavity"*, has been re-simulated and obtained results are compared. 2D schematic of the sensor is regenerated in figure 3.4.

Table 3.1: Geometric parameters of the sensor [8].

Parameters	Indication	Value (nm)
Outer elliptical resonator's long axis length	R1	300
Outer elliptical resonator's short axis length	R2	140
Inner elliptical resonator's long axis length	r1	150
Inner elliptical resonator's short axis length	r2	70
Side length of SRR	l	480
Height of rectangular stubs	h	60
Coupling distance	d	10
Width of MIM waveguide	w	50
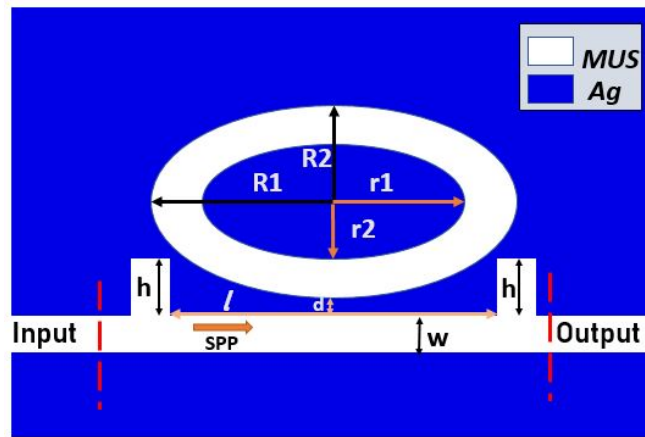
Figure 3.4: Schematic of an RI sensor proposed by Su et al. [8].

The geometric parameters listed in table 3.1, are used to re-simulate the sensor's transmission profile utilizing 2D *FEM* scheme in COMSOL Multiphysics. Steps of the simulation process are shown in figure 3.5.
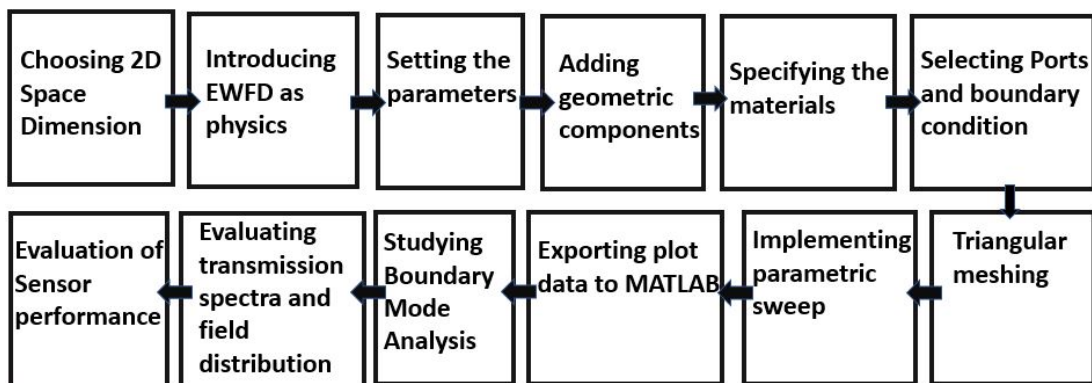
Figure 3.5: The simulation steps are shown in a flow chart.

At start, the space dimension is set to 2D and the electromagnetic wave frequency domain (EWFD) is chosen as the physics. The geometric layout is built using simple

building blocks after defining geometric parameters globally. Silver (Ag) and air are placed in different domains according to the design of the sensor. Scattering boundary condition is applied to all boundaries except input and output ports. The system is discretized with triangular meshing as shown in figure 3.6b. The spectral properties of transmission and field distribution are evaluated using boundary mode analysis. Finally, computed data of transmittance is exported to MATLAB for further investigation of sensor performance parameters.


(a)   (b)
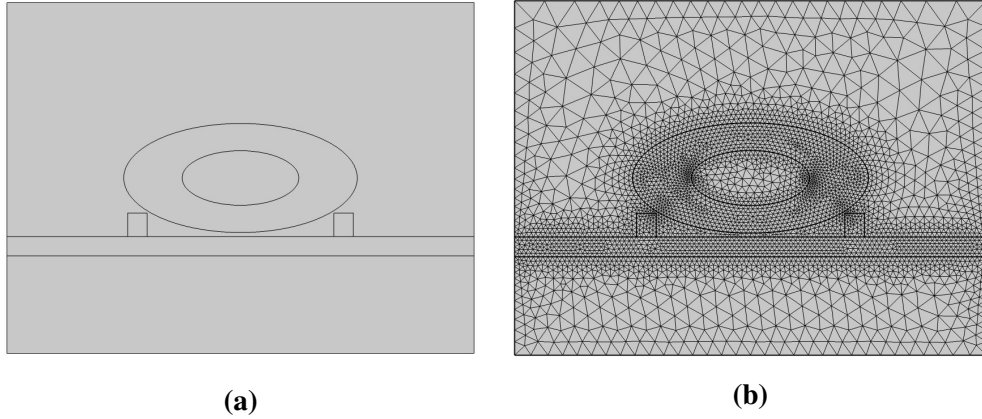
Figure 3.6: 2D view of (a) geometric structure and (b) mesh structure in COMSOL Multiphysics.

The 2D profile of the re-simulated refractive index sensor is presented in figure 3.6. Transmission spectrum of the re-simulated work for different *MIM* configurations, is compared with the published work [8] in figure 3.4. E-field distribution of the system is shown in figure 3.8.

(a)   (b)
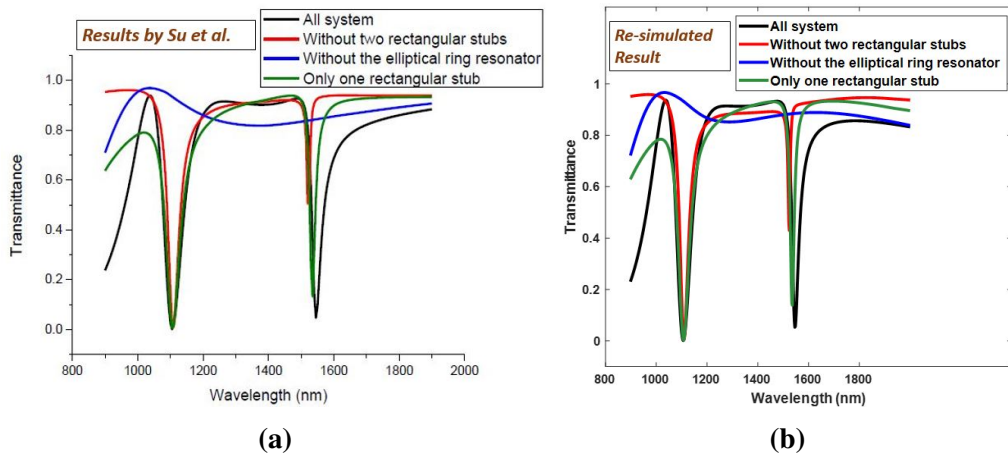
Figure 3.7: Transmission spectrum when R1 = 300 nm, R2 = 140 nm, r1 = 150 nm, r2 = 70 nm, d = 10 nm, l = 480 nm, and h = 60 nm, by (a) Su et al. [8], (b) resimulated work.

24
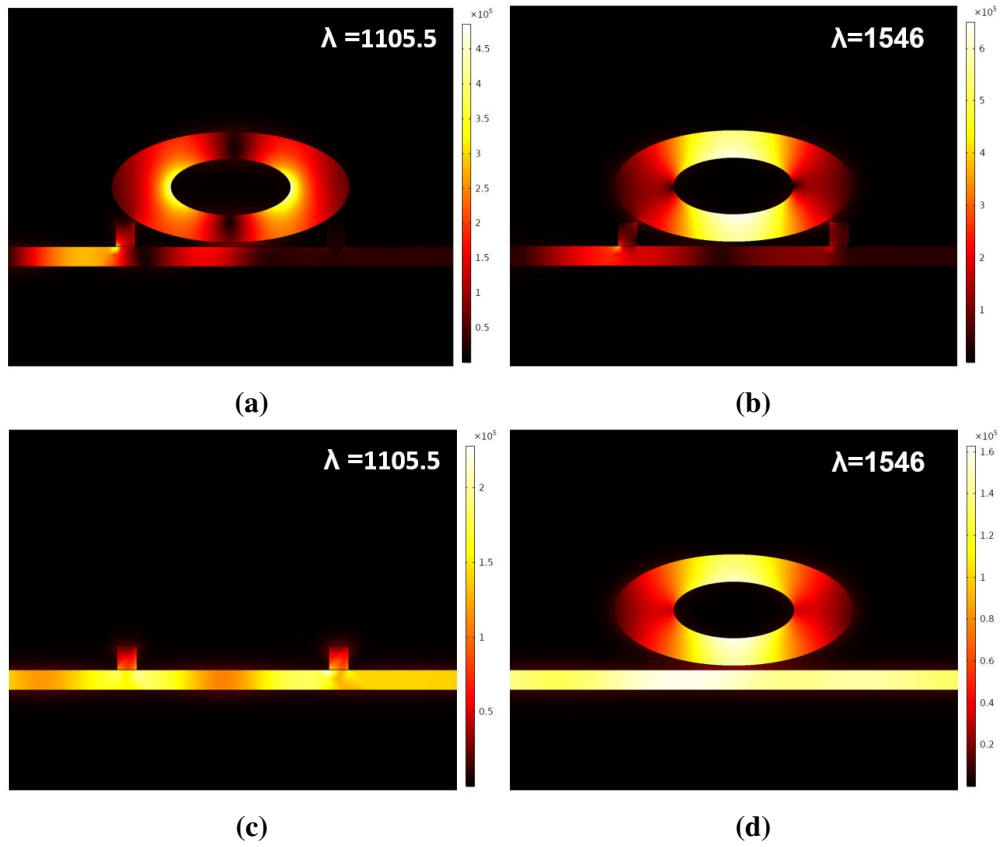
Figure 3.8: E-field distribution of the whole system at (a) $\lambda_{res} = 1105.5nm$ and (b) $\lambda_{res} = 1546nm$, and c) without two rectangular stubs at $\lambda_{res} = 1105.5nm$ and d) without the eliptical ring resonator at $\lambda_{res} = 1546nm$.
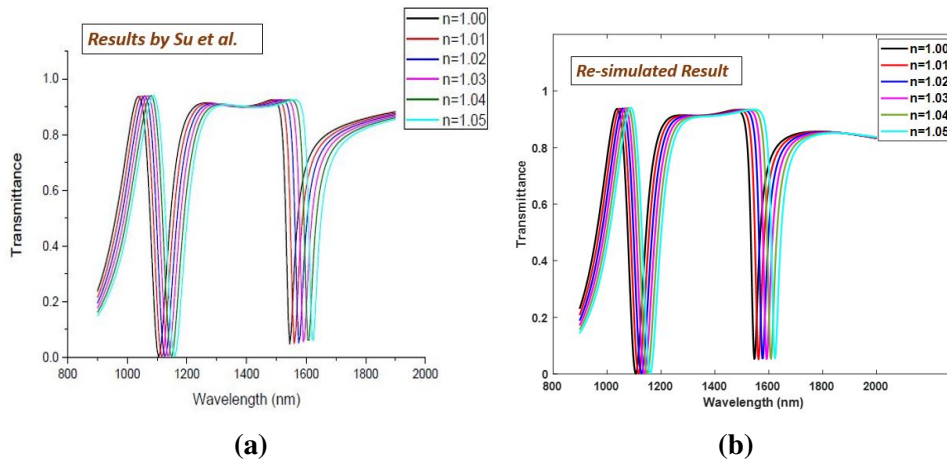
Figure 3.9: Transmission spectrum by (a) Su et al. [8], (b) resimulated work.

Table 3.2: Comparison between the re-simulated results and the published results from Su et al. [8].

	λ_{res} (nm)		Maximum Sensitivity (nm/RIU)
	Dip I	**Dip II**	
Su et al.	1105	1545.5	1550
Re-simulated in COMSOL	1105.5	1546	1540
Percentage of error	0.045%	0.045%	0.645%

The resonant dips of figure 3.9a and figure 3.9b display redshift as refractive index, n, increases. The maximum difference between the dips from re-simuation results and published results, is insignificant (0.5 nm). As recorded in table 3.2, the percentage of difference in terms of sensitivity is 0.645%, which is still negligible to consider. It is evident that the results obtained from the re-simulation validate the simulation procedure of the COMSOL Multiphysics. Therefore, proposed designs in Chapter 4 have been simulated following similar procedures.

Chapter 4

RI Sensor Designs, Performance Analysis, and Applications

One of the key goals is to design a refractive index sensor with better performance. The structural parameters affect the performance metrics of refractive index-based sensors. The aim is to find a better sensor design topology and a better collection of design parameters to improve performance. As a result, optimizing structural parameters is a critical design approach for achieving the best possible result. Enhancement of the light-matter interaction, this time, targets nano-dots at high E-filed confined areas; a recent trend in refractive index-based sensors has been discovered to improve performance metrics. Rectangular and double concentric ring resonators have been studied as resonator designs. The sensor as a food adulterant detector is an example of the use of a refractive index sensor. The tolerance of the design and fabrication method is also discussed.

4.1   Sensor Design with a Square Ring Resonator

4.1.1   Basic Structure

Figure 4.1 shows a two-dimensional (2D) diagram of the proposed plasmonic sensor structure, consisting of a *MIM* waveguide, a laterally coupled square ring resonator (SRR) with a diagonally inserted nano-slit on two opposite sides of the square and a middle rectangular cavity. Several nano-dots (NDs) of silver (Ag) are also mounted on the SRR. The green area of the geometry represents the silver ($\in_m$) layer in the model, and the white area shows the material of unknown refractive index (n) that will be sensed. In table 4.1, all of the model parameters are displayed.

Six NDs with a period (Λ) of 3r are located in l2 of the cavity, where r is the radius of the NDs. A *MIM* bus waveguide couples the square ring resonator sideways. Through placing the NDs in the cavity, the sensor output is measured. Ag is chosen because it
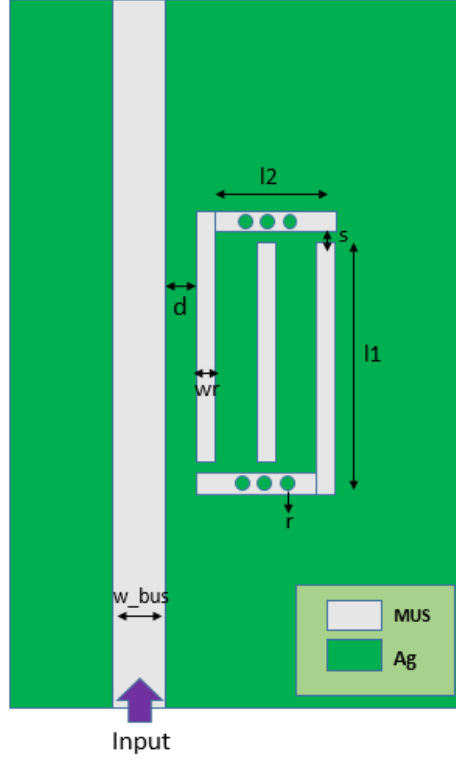
Figure 4.1: Schematic of the proposed *MIM* resonator design.

has a marginal imaginary component of near-infrared (NIR) relative permittivity that results in low energy consumption than gold and copper. Using the finite element method (*FEM*) with a scattering boundary condition, the transmission spectrum and E-field distributions are computed.

Table 4.1: List of the initial structural parameters.

Parameters	Symbol	Values	Unit
Bus waveguide width	w_{bus}	50	nm
Width of rectangle cavities	wr	25	nm
Height of the SRR	l1	310	nm
Side length of the SRR	l2	110	nm
Radius of nanorods	r	7.5	nm
Distance between the bus waveguide and SRR	d	30	nm
Width of nano-slit	s	10	nm

4.1.2 Initial Simulation Results

To assess the efficiency of the novel plasmonic sensor, *FEM* approach is utilized for modeling of the proposed structure. The blue curve represents the transmission spectrum of the structure in figure 4.2. The structural parameters are set to l1 = 310 nm, l2

= 110 nm, r = 7.5 nm, and n = 1.00 for initial simulation. One very sharp resonance dip occurs in the transmission spectrum at 1562 nm, as can be observed. The *FWHM* of the resonance dip is about 22.64 nm.
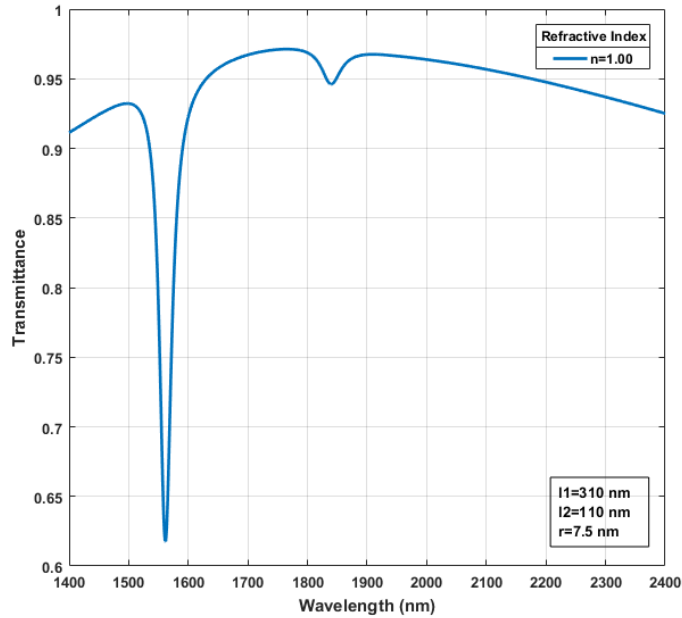
Figure 4.2: The transmittance spectrum of the structure for refractive index n=1.00.

Figure 4.3 shows the $|Hz|$ field distribution of the proposed structure with initial structural parameters for different wavelengths. The refractive index of MUS is adjusted from 1.00 to 1.1 with a 0.025 interval using the same structural parameters. The transmittance dip moves from left to right as the refractive index changes, resulting in a redshift, as seen in figure 4.4a. As seen in figure 4.4b diagram, the resonant wavelength varies roughly linearly as the refractive index changes. For the resonance dip, the structure has a sensitivity of 1550 nm/RIU.

It is possible to calculate the refractive index of the material under sensing from the transmission dip wavelength using the linear relationship between the transmission dips and the refractive index.

Figure 4.3: Magnetic field profile $|Hz|$ at a) $\lambda = 1454$ nm b) $\lambda = 1562$ nm c) $\lambda = 1763$ nm d) $\lambda = 1840$ nm.

Figure 4.4: (a) Transmittance profile for varying refractive indices. (b) Resonant wavelength vs refractive index n.

4.1.3 Optimization
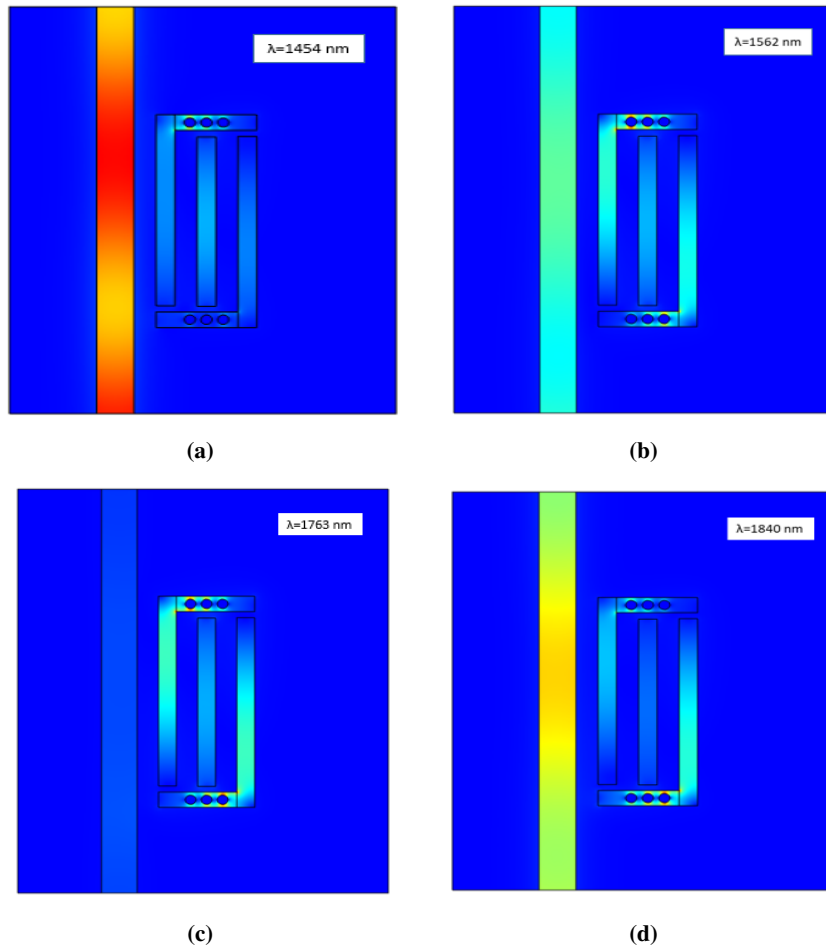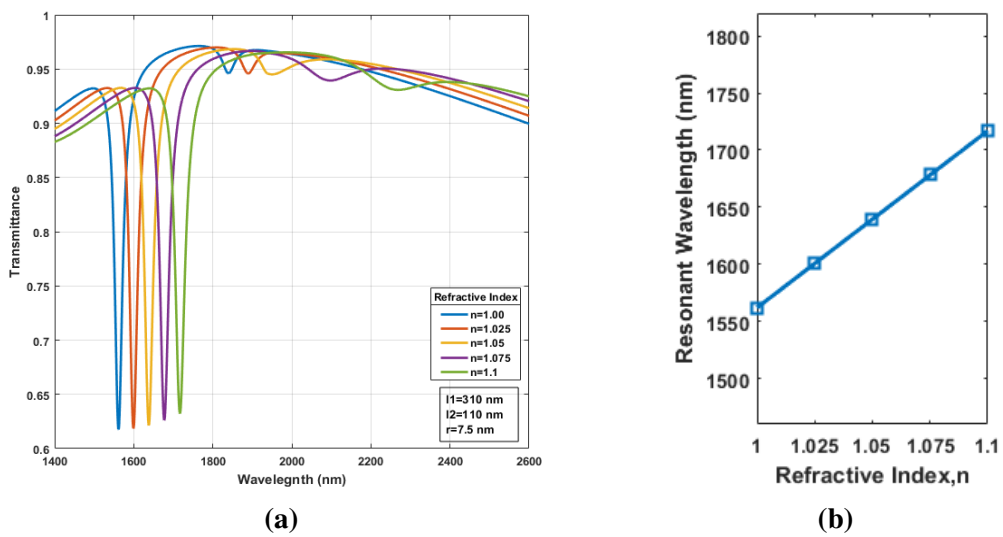
The influence of the three structural parameters (l1, l2, r) on the transmittance curve is evaluated by changing these parameters one at a time while keeping the other parameters constant. An optimization strategy is used to obtain the best possible result from the proposed geometrical structure based on geometrical dependence.
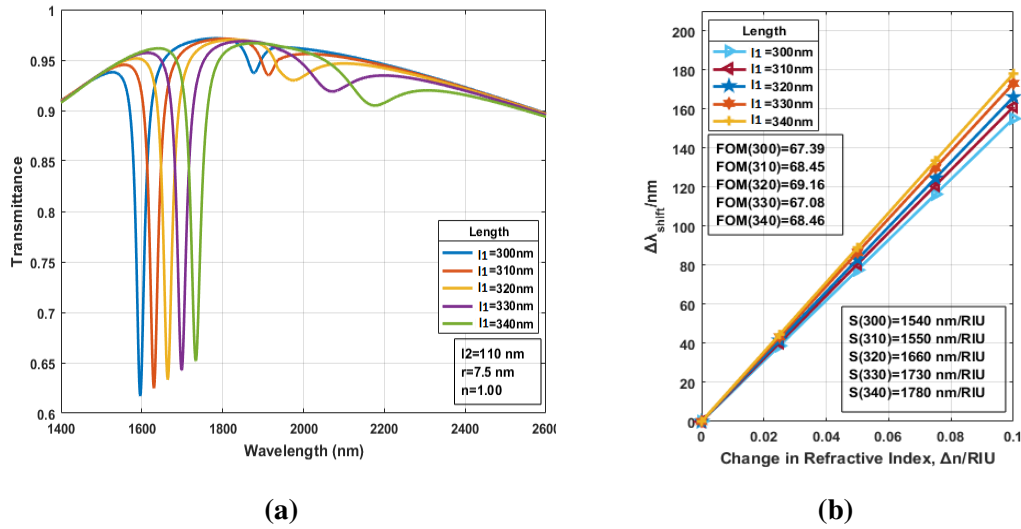

Figure 4.5: (a) Transmission profile of the sensor varying the length of middle cavity l1. (b) Resonant wavelength shift, $\Delta\lambda$ vs Δn.

For refractive index n=1.00, the governing parameter l1 is first modified from 300 to 340 nm in 10 nm increments, while the other two parameters (l2 = 110 nm, r = 7.5 nm) remain unchanged. Figure 4.5a confirms that, as l1 increases, the resonant dip undergoes a redshift. With different values of length (l1) for the dip, figure 4.5b indicates the resonance dip change ($\Delta\lambda$) as a function of refractive index transformation (Δn).

The findings indicate that increasing l1 may increase structural sensitivity. The maximum sensitivity of 1780 nm/RIU is registered when the length l1 = 340 nm is used, significantly higher than the sensor configuration of l1 = 320 nm. However, a narrower *FWHM* and a deeper resonance spectrum with a high *FOM* are needed to detect a transmittance dip precisely. As a result, the length (l1) of the proposed structure has been set to 320 nm, resulting in a nominal sensitivity of 1660 nm/RIU and an average *FOM* of 69.16. The parameter l2 (side length of the SRR) is varied while the other parameters are left unchanged to see how it affects device performance. The transmittance of the dip increases as l2 increases, as seen in figure 4.6a. A redshift with increasing l2 is experienced in the transmittance spectrum. Figure 4.6b suggests that, at l2 = 140 nm,

31

the structure offers a maximum 1710 nm/RIU sensitivity and corresponding *FOM* of 74.34 for the dip.
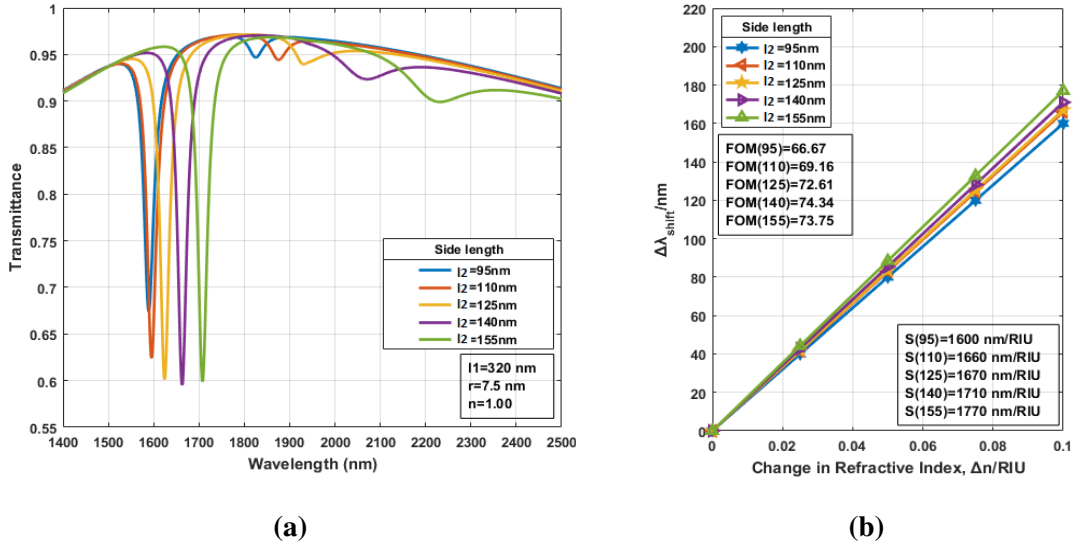
Figure 4.6: Transmittance profile for different values of l2 (b) Resonance dip shift as a result of change in the refractive index Δn.

The transmission spectra in figure 4.7a shows redshift with increasing radius of nanorods, r. Figure 4.7b shows that the SRR configuration with r = 10 nm has the strongest *FOM* of 85.17. As a result, we have the required sensitivity, structure scale, and power transmission values by selecting r=10 nm. The optimized sensitivity recorded is 2470 nm/RIU. These values are higher than those recorded in some recent *MIM*-based studies and should satisfy chemical/sensing requirements.The entire optimization process is summarized in table 4.2. Using the optimization approach, the sensitivity of the structure and *FOM* increase by 59.35 percent and 24.42 percent, respectively, from their original values.

The high sensitivity of the proposed structure opens up developing covenant optical sensors for integrated photonic circuits. Figure 4.8 plots the transmittance result with all structural parameters set to their optimal values to verify the optimized answer. Also, the $Q - factor = \frac{\lambda_{res}}{FWHM}$ of the given schematic is 80.07.
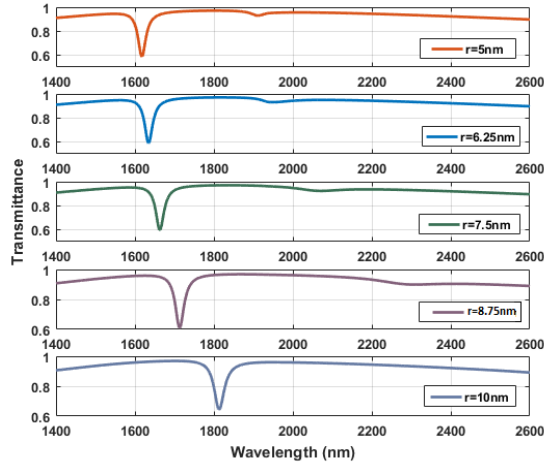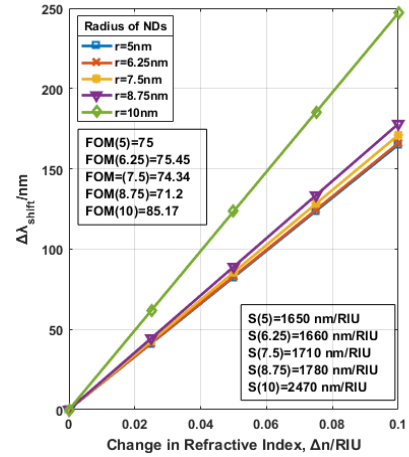
(a)   (b)

Figure 4.7: (a) Transmission profile for varying r. (b) Resonance dip shift as a result of change in the refractive index Δn.

Table 4.2: Summary of sensitivity and *FOM* of the proposed design.

Parameters	Initial value (nm)	Optimized value (nm)	Sensitivity (nm/RIU)		Increased sensitivity (%)	FOM		Increased FOM (%)
			Initial	Final		Initial	Final	
l1	310	320	1550	1660	7.09	68.45	69.17	1.03
l2	110	140	1660	1710	10.32	69.16	74.34	8.6
r	7.5	10	1710	2470	59.35	74.34	85.17	24.42
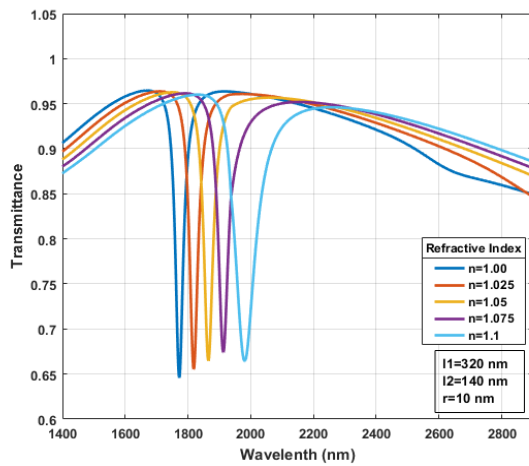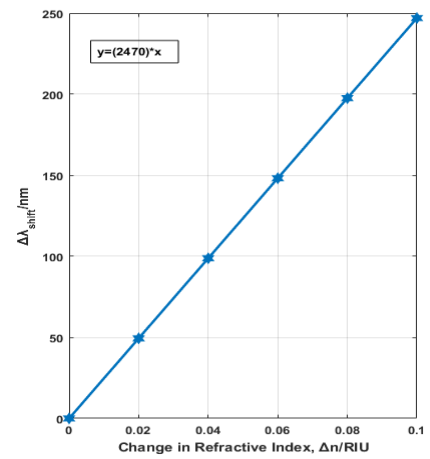
(a)   (b)

Figure 4.8: (a) Transmission profile of the plasmonic structure with l1 = 320 nm, l2 = 140 nm, and r = 10 nm for various refractive indices. (b) Shift in the resonant dip with varying refractive index.

4.1.4 Application as a Food Adulterant Detector

Detecting adulteration of food is one of the versatile uses of the refractive index sensor, which has a wide range of applications. Adulterant identification in pure honey is used as an example of identifying food adulterations in this article. Honey is a complex natural food that provides many health benefits to humans. Adulterant honey was made by diluting three different types of sugar adulterants (fructose, glucose, and sucrose) into pure honey at various concentrations (2%, 4%, 6%, 8%, and 10%). For all samples, the change of the resonance dip was plotted as a function of the concentration of adulterants in pure honey. The key aim of this research is to concentrate on refractive index sensing capability in order to tackle the issue of pure honey adulteration.

For varying concentrations of adulterants, the resonance dip shifts with the refractive index. In figure 4.9, the RI sensor reaction to concentration difference of adulterated honey with three forms of sugar adulterant, namely fructose, glucose, and sucrose, is shown. All of the samples have their own narrow dips in the transmittance curves. As seen in figure 4.9, the dips expose their resonance wavelengths. The change in resonance wavelengths for different samples is due to differences in refractive index [42]. The refractive index of the medium has been estimated to be between 1.351 and 1.353 [43]. Pure honey has a resonance wavelength of 3225-3226 nm for this structure. The association of adulterated honey with the Ag surface resulted in a reduction in the resonance wavelength and a change to the left in the resonance dips.

The change of minimum resonance wavelengths of adulterated honey from pure honey can be determined based on these results. By only physically measuring on sugar adulterated honey, the sensor reveals positive results by getting many explicit wavelength variations. The identification capacity of sugar adulterants into pure honey is implied by the change between the resonance wavelengths of adulterated honey. In reality, the sensing surface of the sensor is extremely sensitive towards refractive index of the medium in which it is placed. It has the ability to monitor variations in surface properties. Figure 4.10 shows a plot of refractive index versus adulterant concentration. The refractive index of pure honey, which includes 0% adulterant volume, is 1.3533, which is the largest. The refractive index decreases as the amount of adulterants in pure honey increases by 2% until it reaches 10%. All of the information gathered can be used as a significant parameter in the development of a reliable sensor to distinguish between pure and impure honey.
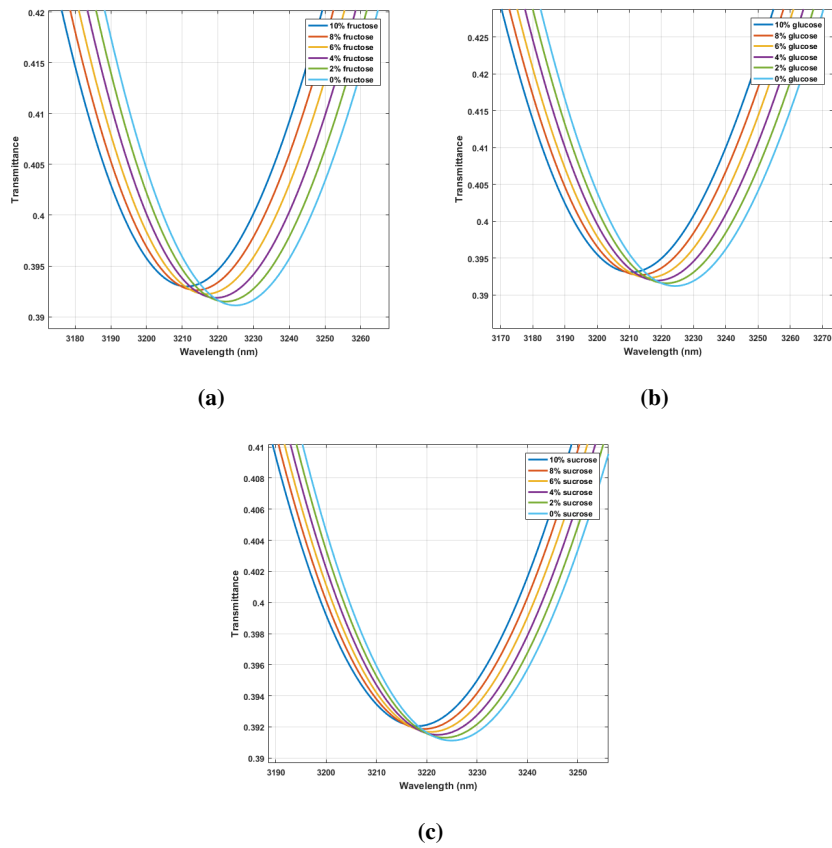
Figure 4.9: Transmittance curves for (a) fructose, (b) glucose and (c) sucrose adulterated honey.
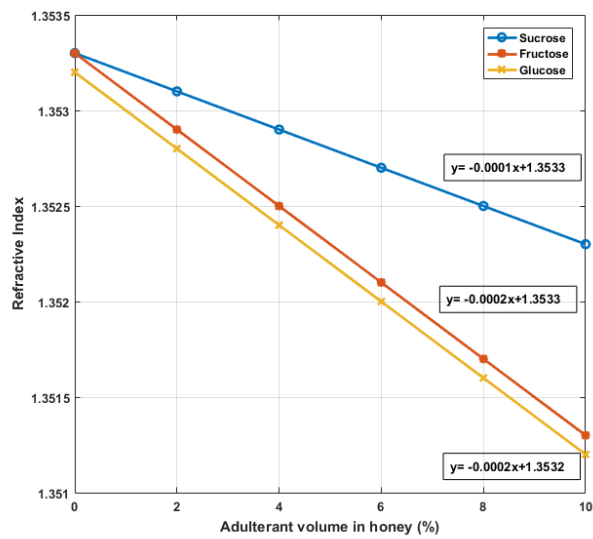
Figure 4.10: Refractive Indices vs. adulterant concentrations.

4.2 Sensor Design with Concentric Double Ring Resonator

4.2.1 Basic Structure

Two dimensional schematic views of the proposed refractive index sensor is shown in figure 4.11. The structure is designed with a concentric double ring resonator consisting of a square ring resonator (SRR) and a circular ring resonator (CRR), coupled to the input-output waveguide with a stub. The area shaded blue in figures 4.11a and 4.11b is silver (ϵ_m), and the gray shaded area denotes the cavities of the *MIM* waveguide. The cavities are infused with the material whose refractive index (n) is to be sensed, while this material under sensing (MUS) has the properties of an insulator. Three pairs of silver (Ag) NDs are loaded to the high E-filed confined area to enhance the performance of the proposed design as designated in figure 4.11b. The initial structural parameters of the device are shown in table 4.3.
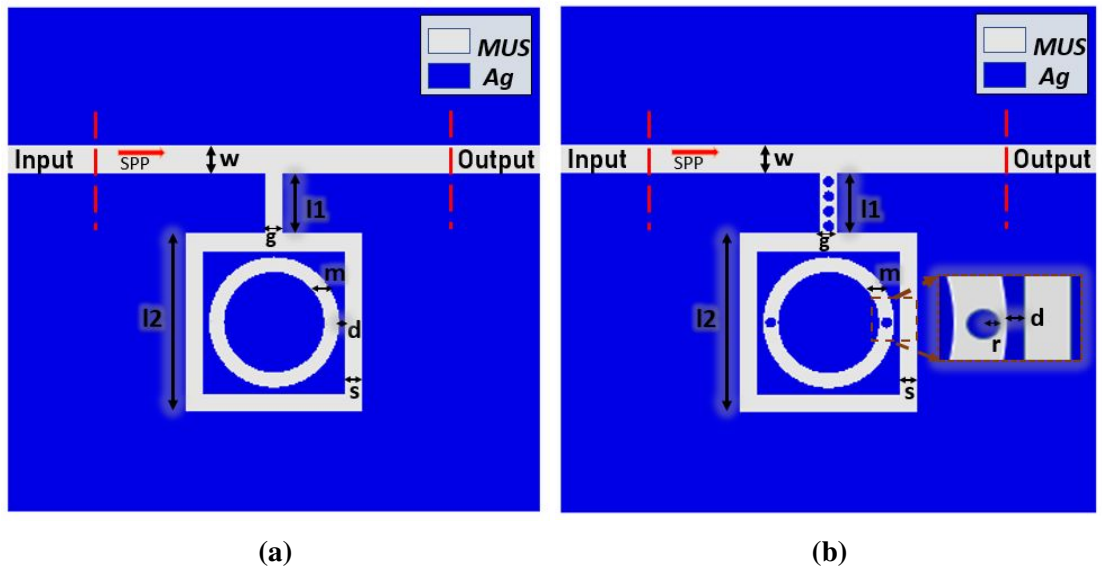
Figure 4.11: Schematic view of a RI sensor with (a) regular cavities (b) with nanodot-decorated cavities.

Table 4.3: Summary of the initial simulation model parameters.

Parameters	Indication	Value (nm)
Width of the waveguide	w	50
Length of the stub	l1	100
Width of the stub	g	30
SRR width	s	30
Side length of SRR	l2	450
Width of CRR	m	25
Distance between SRR and CRR	d	10

4.2.2 Initial Simulation Results

When Refractive Index, n = 1.00
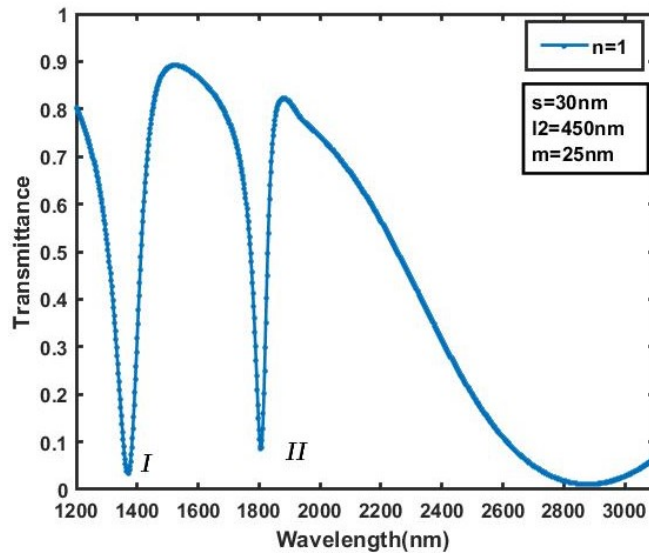
Figure 4.12: The transmission spectrum of SPP for standard design with structural parameters mentioned in table 4.3.

The standard design was simulated for the visible and near-infrared wavelength ranges, with the initial parameters summarized in table 4.3. The simulation displays two asymmetric resonance dips at 1370 nm and 1806 nm when the material refractive index is 1, as shown in figure 4.12. In figures 4.13a and 4.13b E-field distribution of the standard design is shown at resonant wavelengths. The changes in *SPP* propagation after placing NDs in the high E-field concentration region with a radius of 6 nm can be seen in figures 4.13c and 4.13d, at resonant wavelength 1390 nm and 1844 nm, respectively.
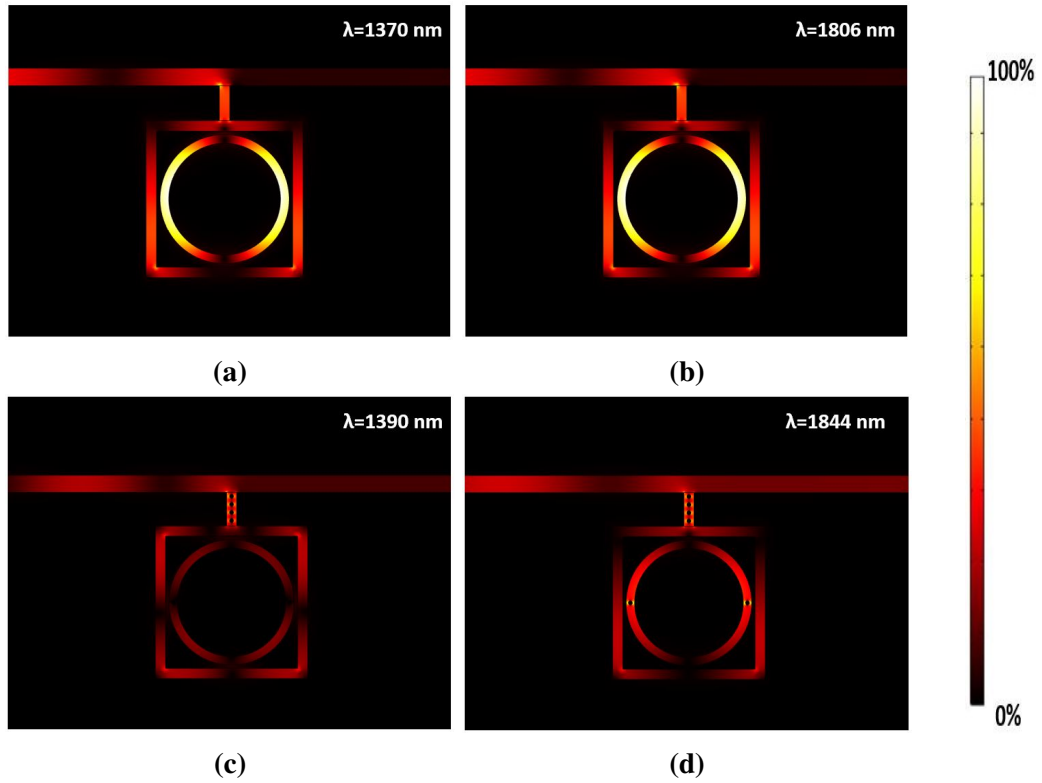
Figure 4.13: E-field distribution at resonant wavelength, (a) $\lambda_{res} = 1370nm$ and (b) $\lambda_{res} = 1806nm$ with Standard design and (c) $\lambda_{res} = 1390nm$ and (d) $\lambda_{res} = 1844nm$ with NDs placed.

With Varying Refractive Index, n = 1.00 to n = 1.1
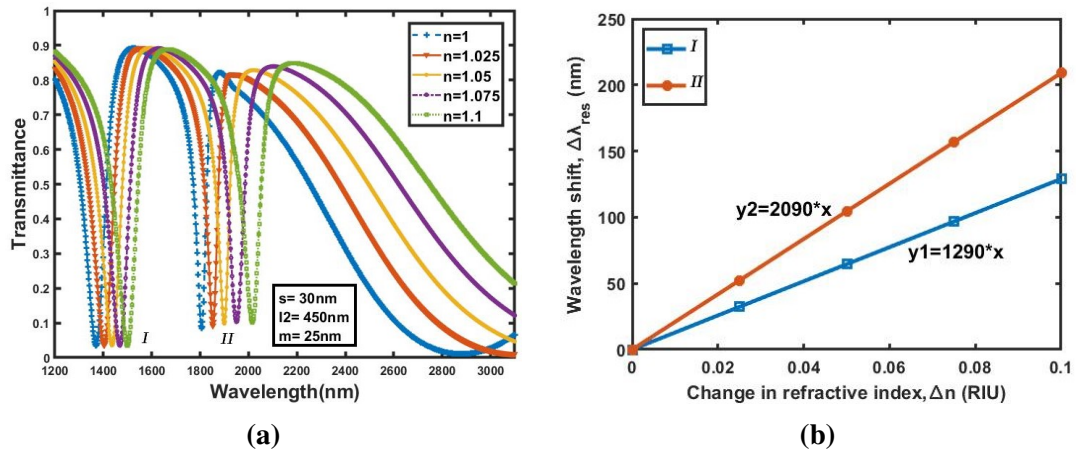
Figure 4.14: (a)Transmission profile for varying refractive index (n). (b) Change in λ_{res} vs. refractive index change (Δn).

Figure 4.14a represents the transmission spectra of the standard design for different MUS with n=1 to 1.1 having intervals of 0.025. Both dips experience red shift with increasing n. The change in resonance wavelength with respect to the variation in

refractive index is depicted in figure 4.14b. The initial sensitivity of the standard structure is 1290 nm/RIU for dip I and 2090 nm/RIU for dip II when $\Delta n = 0.1$. Initially achieved *FOM* of dip I and dip II are 12.95 and 41.6, respectively while the *Q-factor* values are 13.76 for dip I and 35.94 for dip II.

4.2.3 Optimization

Inducing NDs
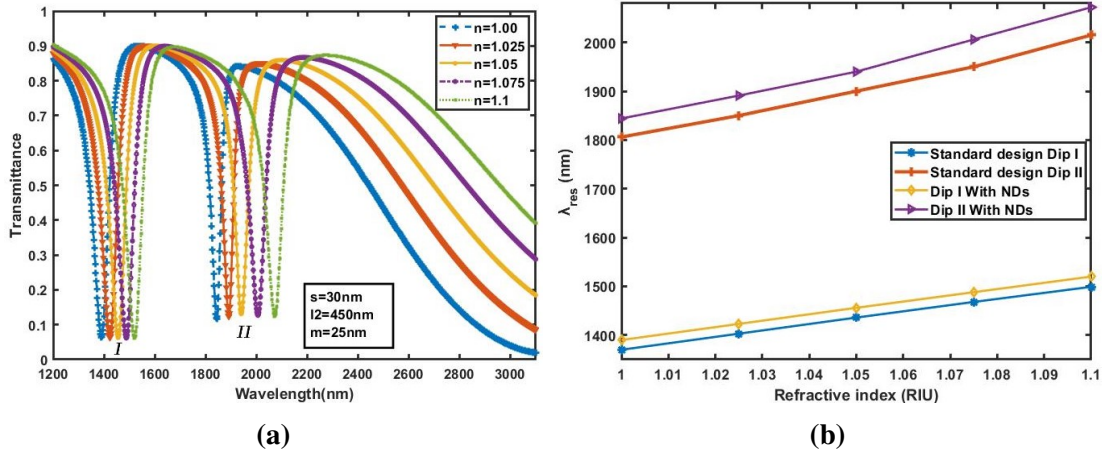
Figure 4.15: (a)Transmittance spectrum of the NDs decorated structure. (b) λ_{res} vs. refractive index (n).

The placement of NDs in the high E-field region has a direct effect on the sensor performance. A shift of λ_{res} to a longer wavelength is observed after decorating the structure with NDs, as shown in figure 4.15b. Transmission profile of the structure with NDs is appeared in figure 4.15a. A comparison between the performance parameters of the standard structure and the structure with NDs is summarized in table 4.4. As seen in the table, all the performance metrics get improved due to the placement of NDs. The sensitivity increases 9.09% for dip II compared to the standard layout. Similarly *FOM* and *Q-factor* (n = 1) for dip II increase by 19.33 % and 11.71% respectively.

Table 4.4: Sensor performance of the structure with NDs

Performance metrics	Standard Design		NDs with r = 6 nm placed in the high E-field region		Percentage increase	
	I	II	I	II	I	II
Sensitivity (nm/RIU)	1290	2090	1300	2280	0.77%	9.09%
FOM	12.95	41.6	17.18	49.64	32.66%	19.33%
Q-Factor (for n=1)	13.76	35.94	18.37	40.15	33.5%	11.71%

Optimization of the Geometrical Parameters

Figure 4.16: (a) Transmission characteristics. (b) Sensor performance with variation of s.

The influence of SRR width s on transmission profile of the design is studied keeping other parameters fixed. With increase of the value of s from 20 nm to 40 nm with an interval of 5 nm, the resonance wavelength (λ_{res}) experiences blue shift as presented in figure 4.16a. The calculated results for each value of s imply that sensitivity has an inverse relation with the SRR width,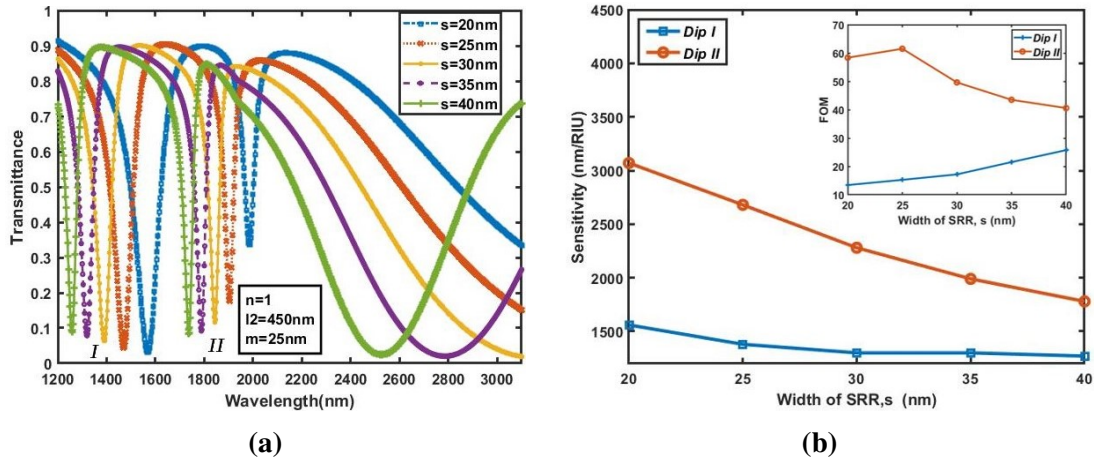 as shown in figure 4.16b. The structure can obtain a maximum sensitivity of 1560 nm/RIU for dip I and 3070 nm/RIU for dip II when s = 20 nm. However, in most cases, with the increase of sensitivity, *FOM* decreases, which is also evident in previous literatures [39]. The inset of figure 4.16b illustrates the nonlinear relationship between *FOM* and s. So, to ensure high sensitivity with moderate *FOM*, s is set at 25 nm which results a maximum sensitivity of 1380 nm/RIU and 2680 nm/RIU for dip I and dip II, respectively. At s = 25 nm, FOM is 15.25 for dip I and 61.52 for dip II.

It is evident from figure 4.17a that with increasing length l2, λ_{res} shows redshift as well as the sensitivity increases. Effect of sensitivity on length l2 is depicted in figure 4.17b, while the inset figure maps the *FOM*. Ensuring high sensitivity with moderate *FOM*, l2 = 500 nm is set as an optimized structural parameter. A maximum sensitivity and *FOM* for optimized setup is reported as 3440 nm/RIU (dip II) and 37.27 (dip II) respectively.

Figure 4.18a shows that the controllable resonant wavelength was achieved by changing the width of the CRR, m. The resonant wavelength faces blue shift for the increment of m. As a result sensitivity decreases for higher values of m but *FOM* increases. Up to m = 35 nm, sensitivity was falling linearly and a high increase in *FOM* can be
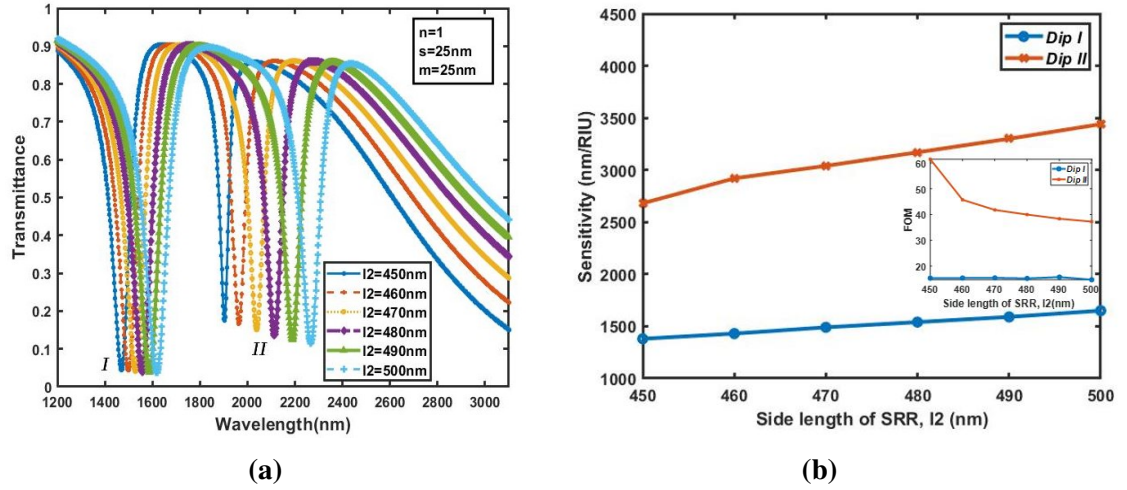
Figure 4.17: (a) Transmission profile. b) Performance metrics for different values of l2.
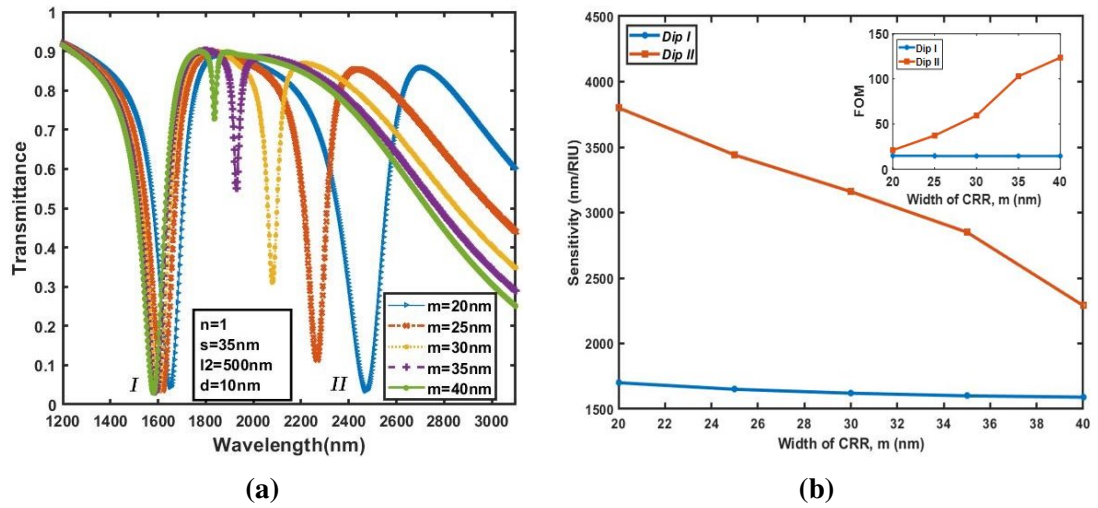
Figure 4.18: (a) Transmission spectra. (b) Change in values of sensitivity and *FOM* with varying CRR width m.

observed, as demonstrated in figure 4.18b and the inset figure. After this point sensitivity drops rapidly but the improvement of *FOM* is comparatively insignificant. So, the structure is optimized by choosing the value of m at 35 nm, providing a maximum sensitivity of 1600 nm/RIU and 2850nm/RIU, and the maximum refractive index sensitivity *FOM* of 14.53 and 105.95 for dip I and dip II, respectively.

The sensitivity of the proposed sensor decorated with NDs is realized when all structural parameters are set to optimal values while varying refractive index n from 1 to 1.1, as illustrated in figure 4.19. The sensitivity of the optimized structure is shown by the slope of y2 and y1 in the inset figure.
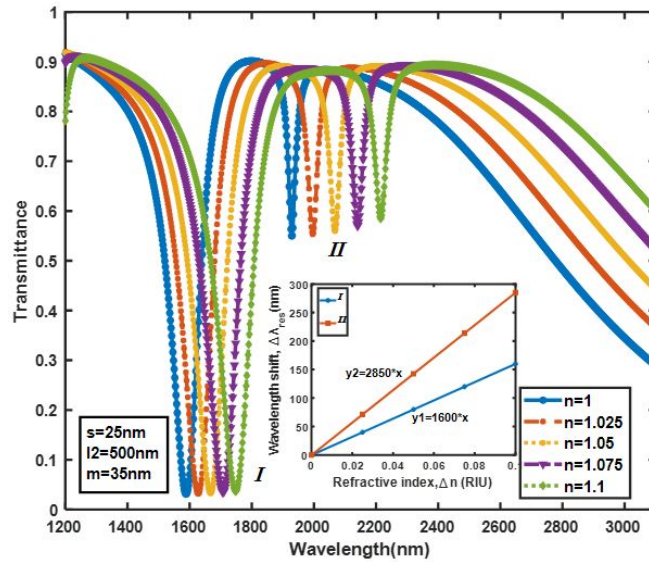
Figure 4.19: Transmission profile of the optimized device.
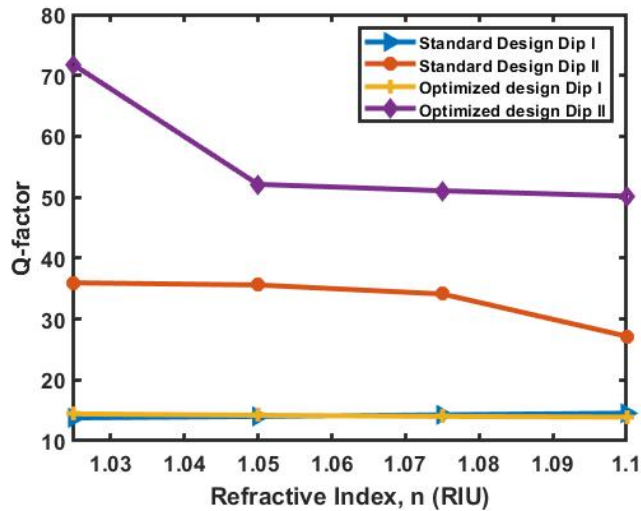
Figure 4.20: *Q-factor* of the optimized device vs. refractive index (n).

Q-factor of the optimized sensor for dip II is way higher than that of the standard layout whereas for the other dip *Q-factor* of the two layouts are almost equal, as shown in figure 4.20. A higher value of *Q-factor* is desirable as it indicates a lower rate of energy loss. Table 4.5 summarizes the performance metrics of the optimized design with comparison to the initial structure. Results suggest that dip II is more suitable for sensing. The sensitivity for dip II increases 36.36% after optimization, when *FOM* experiences an increase of 154.69% and *Q-factor* is increased by 99.53% .

42

Table 4.5: Performance metrics of the proposed sensor.

Performance metrics	Initial design		Optimized design		Percentage increase	
	I	II	I	II	I	II
Sensitivity (nm/RIU)	1290	2090	1600	2850	24.03%	36.36%
FOM	12.95	41.6	14.53	105.95	12.2%	154.69%
Q-Factor (for n=1)	13.76	35.94	14.42	71.71	4.8%	99.53%

4.2.4 Manufacturing Process of the Proposed Sensor

Various maskless techniques with precise resolution, such as focused ion beam milling (FIB) [44], electron beam lithography (EBL) [45], and nanoimprint lithography (NIL) [46] can be utilized for manufacturing proposed device. Electron beam lithography among them offers high resolution and low throughput, therefore it excels in creating custom designs with a resolution under 10 nm.

(a) Ag layer deposition   **(b)** Spin-coating   **(c)** E-beam writing

(d) Developing   **(e)** Chemical etching   **(f)** Resist removal
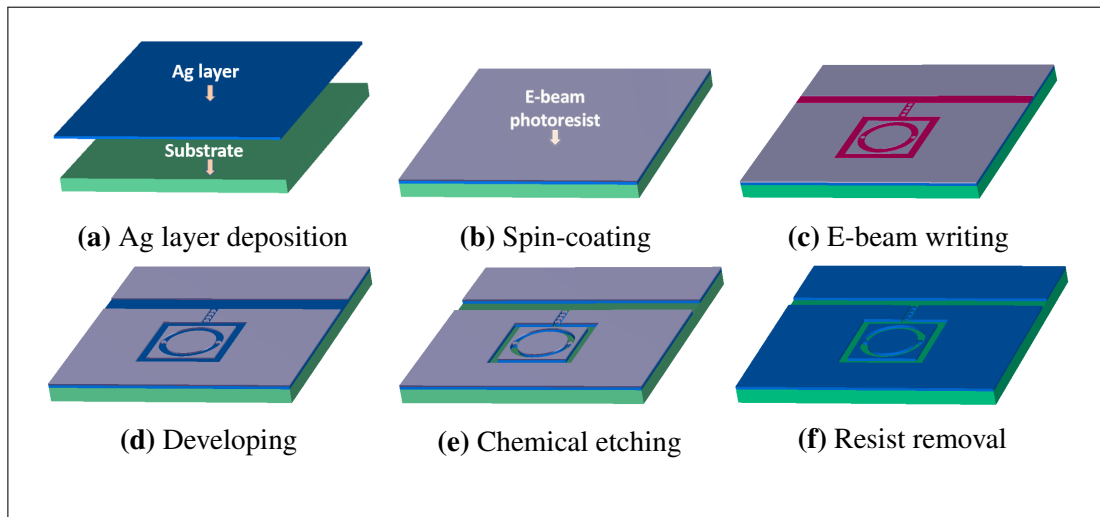
Figure 4.21: Proposed fabrication process for the MIM waveguide plasmonic sensor.

E-beam lithography patterning is a technique for creating custom shapes on a resist by scanning a focused beam of electrons. The resist is an electron-sensitive film spin-coated after a thin coating of Ag is applied on a silica (SiO_2) substrate. The electron beam enables selective removal of either exposed or non-exposed resist area by submerging it in a solvent that is termed as developing process, which results in changing the solubility of the resist. Wet etching removes the undesired metal component from the system. Using diluted nitric acid and water is a suitable technique as it has a high etch selectivity. The schematic illustration of the fabrication is demonstrated in Figure 4.21.

Tolerance Testing of Probable Displacement

Practical manufacturing process can result in a mismatch between the sensor's measurements and their optimized values, which will alter the sensitivity. The effect of placement defects of different NDs in the cavity of the proposed sensor, is investigated. Figure 4.22 displays the E-field intensities for the different alignment of the top four NDs at λ_{res} = 1588 nm, 1589 nm and 1589 nm. As shown, three layouts are studied with NDs centrally aligned, displacement to the left edge, and displacement to the right edge.

(a)   **(b)**   **(c)**
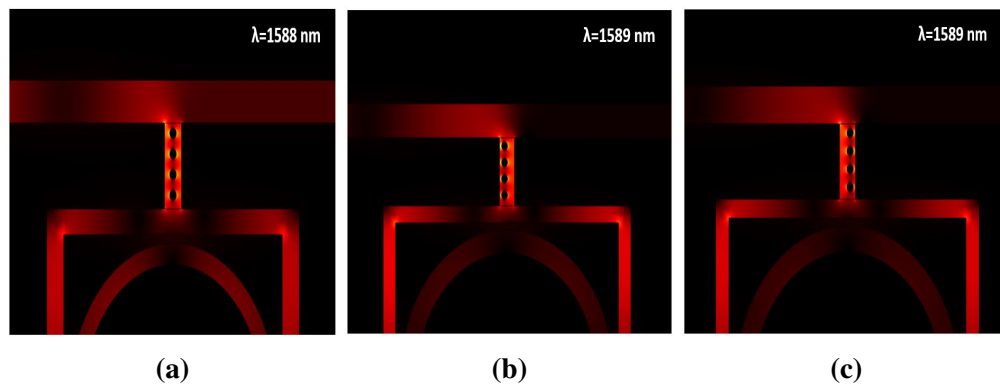
Figure 4.22: E-field distribution of cavity when the top four NDs are (a) centrally aligned, (b) displaced to the left edge and (c) displaced to the right edge.

Similarly displacement of the leftmost and the rightmost ND is examined as shown in Figures 4.23a and 4.23b. The misalignment of ± 25 nm for both the NDs is studied separately.

(a)   **(b)**
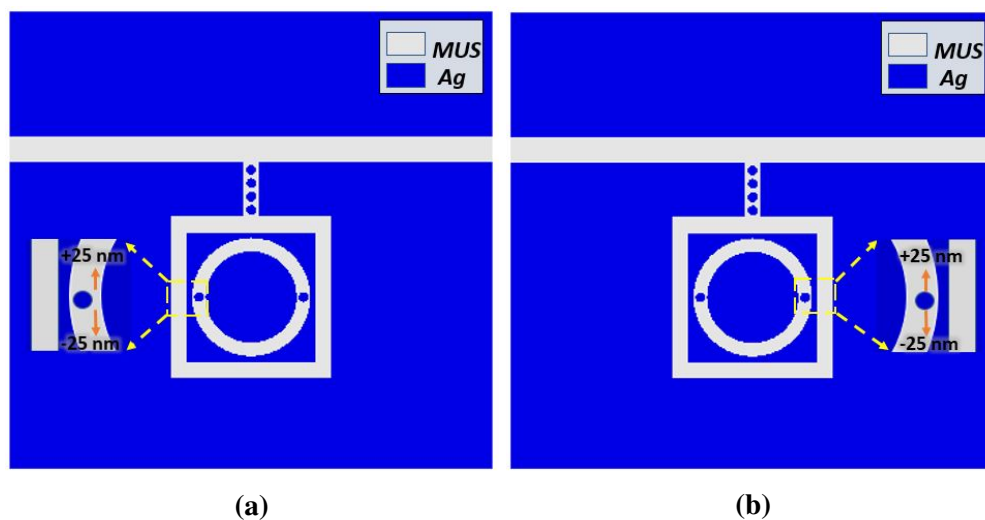
Figure 4.23: Displacement of(a) leftmost and (b) rightmost ND ± 25nm.

Considering all three possibilities of fabrication error recorded in table 4.6, sensitivity do not alter more than 0.625% and 0.701% for dip I and II, respectively. This finding demonstrates the proposed sensor's ability to work under unfavorable conditions, signifying a high degree of tolerance.

Table 4.6: Limit of tolerance for ND location mismatch.

Position of NDs in cavity	Displacement	Dip I (nm/RIU)	Dip II (nm/RIU)	Change in sensitivity (%)	
				Dip I	Dip II
Top four NDs in the stub	Centrally aligned	1600	2850	-	-
	To the right edge	1600	2860	0	0.35
	To the left edge	1600	2860	0	0.35
Leftmost ND in the CRR	0 nm	1600	2850	-	-
	+25 nm	1600	2870	0	0.701
	-25 nm	1590	2860	-0.625	0.35
Rightmost ND in the CRR	0 nm	1600	2850	-	-
	+25 nm	1600	2860	0	0.35
	-25nm	1600	2850	0	0

Chapter 5

Conclusion and Future work

5.1 Conclusion

An investigation is carried out in the hunt for better performing refractive index sensors. E-filed propagation and transmission spectra of the proposed devices are studied using the *FEM* scheme of the COMSOL Multiphysics Software. The variation in resonant wavelength for a unit change in refractive index is called sensitivity. It decides how sensitive a sensor is. To improve sensing capability, structural parameters are optimized one at a time, and nano-dots are filled in areas with high light intensities. *FOM* is a metric that indicates how well a sensor performs in terms of sensitivity and narrow linewidth. The proposed sensors outperform previous *MIM*-based RI sensors in terms of sensitivity and *FOM*, as seen in table 5.1, as compared to some recent works.

This study proposes two plasmonic refractive index sensor structures with enhanced output parameters. One of them is a Metal-Insulator-Metal (*MIM*) waveguide coupled with a square ring resonator with a center rectangular cavity. The SRR is further decorated with a series of silver nano-dots. The structure has an overall sensitivity of 2470 nm/RIU and a *FOM* of 85.17 at optimized parameter values of L1 = 320 nm, L2 = 140 nm, and r = 10 nm. The feasibility of the planned schematic as a food adulterant detector was tested by filling the cavity with adulterated honey.

Another structure is focused on double concentric ring resonator containing a square ring resonator (SRR) and a circular ring resonator (CRR), coupled to a metal-insulator-metal (*MIM*) bus waveguide and a rectangular stub. A maximum sensitivity of 2850 nm/RIU was achieved by the optimized design, and associate figure of merit (*FOM*) and quality factor (*Q-factor*) obtained are 105.95 and 71.71 discreetly. The structure's high tolerance for possible real manufacturing flaws makes it easy-to-manufacture. The compact and basic design of the sensors make them perfect for use in bio-implantable

Table 5.1: Comparison of overall performance metrics of the proposed devices with some previous *MIM*-based devices.

References	Year	Sensitivity	*FOM*
Xie et al. [2]	2015	1562.5	38.6
Zou et al. [47]	2015	3960	-
Tang et al. [32]	2017	1125	75
Yi et al. [48]	2018	1700	60.7
Butt et al. [35]	2019	1367	25
Butt et al. [36]	2020	1240	20
Bazgir et al. [19]	2020	1260	120
Sagor et al. [22]	2020	1556	17.87
Proposed structure I	2021	2470	85.17
Proposed structure II	2021	2850	105.95

on-chip sensing applications.

5.2   Future Work

Two structures of cavity resonator-based RI sensor with *MIM* configuration have been optimized in this work.The following steps can be taken in the future to improve the *MIM*-based plasmonic system.

- To reduce plasmonic sensor's propagation loss, alternative materials with variable doping concentration can be chosen.

- Machine learning can be incorporated into the optimization process.

- Geometric parameters can be fine-tuned to add a fano-like transmission profile.

REFERENCES

[1] Z. Han and S. I. Bozhevolnyi, *Waveguiding with surface plasmon polaritons*. Elsevier B.V., 2014, vol. 4. [Online]. Available: http://dx.doi.org/10.1016/B978-0-444-59526-3.00005-7

[2] Y.-y. Xie, Y.-x. Huang, W.-l. Zhao, W.-h. Xu, and C. He, "A Novel Plasmonic Sensor Based on Metal – Insulator – Metal Waveguide With Side-Coupled Hexagonal Cavity A Novel Plasmonic Sensor Based on Metal – Insulator – Metal Waveguide With Side-Coupled Hexagonal Cavity," vol. 7, no. 2, 2015.

[3] F. Chen and D. Yao, "Realizing of plasmon Fano resonance with a metal nanowall moving along MIM waveguide," *Optics Communications*, vol. 369, pp. 72–78, 2016.

[4] M. R. Rakhshani and M. A. Mansouri-birjandi, "Sensors and Actuators B : Chemical High sensitivity plasmonic refractive index sensing and its application for human blood group identification," *Sensors & Actuators: B. Chemical*, vol. 249, pp. 168–176, 2017. [Online]. Available: http://dx.doi.org/10.1016/j.snb.2017.04.064

[5] Y. Zhang and M. Cui, "Refractive Index Sensor Based on the Symmetric MIM Waveguide Structure," *Journal of Electronic Materials*, vol. 48, no. 2, pp. 1005–1010, 2019.

[6] R. Al, M. Omar, F. Rakibul, and H. Sagor, "Plasmonic Refractive Index Sensor Based on Ring - Type Pentagonal Resonator with High Sensitivity," *Plasmonics*, no. 0123456789, 2021. [Online]. Available: https://doi.org/10.1007/s11468-020-01357-7

[7] M. A. Butt, N. L. Kazanskiy, and S. N. Khonina, "Highly Sensitive Refractive Index Sensor Based on Plasmonic Bow Tie Configuration," no. May, 2020.

[8] H. Su, S. Yan, X. Yang, J. Guo, J. Wang, and E. Hua, "Sensing features of the fano resonance in an MIM waveguide coupled with an elliptical ring resonant cavity," *Applied Sciences (Switzerland)*, vol. 10, no. 15, 2020.

[9] Z. Rashid, A. S. Jon, C. Anu, and L. B. Mark, "Plasmonics: the next chip-scale technology," *Materials Today*, vol. 9, no. 7-8, pp. 20–27, 2006. [Online]. Available: http://www.sciencedirect.com/science/article/pii/S1369702106715723

[10] F. J. Garcia-Vidal, L. Martin-Moreno, T. W. Ebbesen, and L. Kuipers, "Light passing through subwavelength apertures," *Reviews of Modern Physics*, vol. 82, no. 1, pp. 729–787, 2010.

[11] L. Guyot, A.-P. Blanchard-Dionne, S. Patskovsky, and M. Meunier, "Integrated silicon-based nanoplasmonic sensor," *Optics Express*, vol. 19, no. 10, p. 9962, 2011.

[12] W. L. Barnes, A. Dereux, and T. W. Ebbesen, "Surface plasmon subwavelength optics," *Nature*, vol. 424, no. 6950, pp. 824–830, aug 2003. [Online]. Available: http://www.nature.com/articles/nature01937

[13] A. V. Zayats, I. I. Smolyaninov, and A. A. Maradudin, "Nano-optics of surface plasmon polaritons," *Physics reports*, vol. 408, no. 3-4, pp. 131–314, 2005.

[14] D. K. Gramotnev and S. I. Bozhevolnyi, "Plasmonics beyond the diffraction limit," *Nature Photonics*, vol. 4, no. 2, pp. 83–91, 2010. [Online]. Available: http://dx.doi.org/10.1038/nphoton.2009.282

[15] S. A. Maier and H. A. Atwater, "Plasmonics: Localization and guiding of electromagnetic energy in metal/dielectric structures," *Journal of Applied Physics*, vol. 98, no. 1, 2005.

[16] J. J. Burke, G. I. Stegeman, and T. Tamir, "Surface-polariton-like waves guided by thin, lossy metal films," *Physical Review B*, vol. 33, no. 8, pp. 5186–5201, 1986.

[17] E. N. Economou, "Surface plasmons in thin films," *Physical Review*, vol. 182, no. 2, pp. 539–554, 1969.

[18] R. Zia, M. D. Selker, P. B. Catrysse, and M. L. Brongersma, "Geometries and materials for subwavelength surface plasmon modes," *Journal of the Optical Society of America A*, vol. 21, no. 12, p. 2442, 2004.

[19] P. Berini, R. Charbonneau, N. Lahoud, and G. Mattiussi, "Characterization of long-range surface-plasmon-polariton waveguides," *Journal of Applied Physics*, vol. 98, no. 4, 2005.

[20] A. E. Craig, G. A. Olson, and D. Sarid, "Experimental observation of the long-range surface-plasmon polariton," *Optics Letters*, vol. 8, no. 7, p. 380, 1983.

[21] Z. Chen, L. Cui, X. Song, L. Yu, and J. Xiao, "High sensitivity plasmonic sensing based on Fano interference in a rectangular ring waveguide," *Optics Communications*, vol. 340, pp. 1–4, 2015.

[22] R. H. Sagor, M. F. Hassan, S. Sharmin, T. Z. Adry, and M. A. R. Emon, "Numerical investigation of an optimized plasmonic on-chip refractive index sensor for temperature and blood group detection," *Results in Physics*, vol. 19, p. 103611, 2020.

[23] D. Fleischman, L. A. Sweatlock, H. Murakami, and H. Atwater, "Hyper-selective plasmonic color filters," *Optics Express*, vol. 25, no. 22, p. 27386, 2017.

[24] J. Shibayama, H. Kawai, J. Yamauchi, and H. Nakano, "Analysis of a 3D MIM waveguide-based plasmonic demultiplexer using the TRC-FDTD method," *Optics Communications*, vol. 452, no. July, pp. 360–365, 2019. [Online]. Available: https://doi.org/10.1016/j.optcom.2019.07.069

[25] Y. Y. Xie, C. He, J. C. Li, T. T. Song, Z. D. Zhang, and Q. R. Mao, "Theoretical Investigation of a Plasmonic Demultiplexer in MIM Waveguide Crossing with Multiple Side-Coupled Hexagonal Resonators," *IEEE Photonics Journal*, vol. 8, no. 5, 2016.

[26] X. Hu, C. Xin, Z. Li, and Q. Gong, "Ultrahigh-contrast all-optical diodes based on tunable surface plasmon polaritons," *New Journal of Physics*, vol. 12, 2010.

[27] C. Haffner, W. Heni, Y. Fedoryshyn, J. Niegemann, A. Melikyan, D. L. Elder, B. Baeuerle, Y. Salamin, A. Josten, U. Koch, C. Hoessbacher, F. Ducry, L. Juchli, A. Emboras, D. Hillerkuss, M. Kohl, L. R. Dalton, C. Hafner, and J. Leuthold, "All-plasmonic Mach-Zehnder modulator enabling optical high-speed communication at the microscale," *Nature Photonics*, vol. 9, no. 8, pp. 525–528, 2015. [Online]. Available: http://dx.doi.org/10.1038/nphoton.2015.127

[28] M. A. Butt, S. N. Khonina, and N. L. Kazanskiy, "Metal-insulator-metal nano square ring resonator for gas sensing applications," in *Waves in Random and Complex Media*. Taylor & Francis, 2019, vol. 0, no. 0, pp. 1–11. [Online]. Available: https://doi.org/17455030.2019.1568609

[29] S.-y. Tseng, S.-y. Li, S.-y. Yi, A. Y. Sun, D.-y. Gao, and D. Wan, "Food Quality Monitor : Paper-Based Plasmonic Sensors Prepared Through Reversal Nanoimprinting for Rapid Detection of Biogenic Amine Odorants Food Quality Monitor : Paper-Based Plasmonic Sensors Prepared Through Reversal Nanoimprinting for Rapid Detection ," 2017.

[30] M. F. Hassan, I. Tathfif, M. Radoan, and R. H. Sagor, "A concentric double-ring resonator based plasmonic refractive index sensor with glucose sensing capabil-

ity," *IEEE Region 10 Annual International Conference, Proceedings/TENCON*, vol. 2020-Novem, pp. 91–96, 2020.

[31] M. Bahramipanah, M. S. Abrishamian, S. A. Mirtaheri, and J. M. Liu, "Ultracompact plasmonic loop-stub notch filter and sensor," *Sensors and Actuators, B: Chemical*, vol. 194, pp. 311–318, 2014. [Online]. Available: http://dx.doi.org/10.1016/j.snb.2013.12.084

[32] Y. Tang, Z. Zhang, R. Wang, Z. Hai, C. Xue, W. Zhang, and S. Yan, "Refractive index sensor based on Fano resonances in metal-insulator-metal waveguides coupled with resonators," *Sensors*, vol. 17, no. 4, p. 784, 2017.

[33] E. Rafiee, R. Negahdari, and F. Emami, "PT SC," *Photonics and Nanostructures - Fundamentals and Applications*, 2018. [Online]. Available: https://doi.org/10.1016/j.photonics.2018.11.006

[34] M. A. Butt, S. N. Khonina, and N. L. Kazanskiy, "Plasmonic refractive index sensor based on M-I-M square ring resonator," *2018 International Conference on Computing, Electronic and Electrical Engineering, ICE Cube 2018*, pp. 1–4, 2019.

[35] ——, "Plasmonic refractive index sensor based on metal–insulator-metal waveguides with high sensitivity," *Journal of Modern Optics*, vol. 66, no. 9, pp. 1038–1043, 2019. [Online]. Available: https://doi.org/10.1080/09500340.2019.1601272

[36] ——, "l P re of," *Optik - International Journal for Light and Electron Optics*, p. 163655, 2019. [Online]. Available: https://doi.org/10.1016/j.ijleo.2019.163655

[37] ——, "A multichannel metallic dual nano-wall square split-ring resonator : design analysis and applications," 2019.

[38] M. R. Rakhshani, "Optical refractive index sensor with two plasmonic double-square resonators for simultaneous sensing of human blood groups," *Photonics and Nanostructures - Fundamentals and Applications*, vol. 39, p. 100768, 2020. [Online]. Available: https://doi.org/10.1016/j.photonics.2020.100768

[39] N. L. Kazanskiy and M. A. Butt, "Enhancing the sensitivity of a standard plasmonic MIM square ring resonator by incorporating nanodots in the cavity," vol. 12, no. 1, pp. 1–3, 2020.

[40] F. Hassan, R. H. Sagor, I. Tathfif, and K. S. Rashid, "An Optimized Dielectric-Metal-Dielectric," vol. XX, no. XX, pp. 1–9, 2020.

[41] R. Ameling, L. Langguth, M. Hentschel, M. Mesch, P. V. Braun, and H. Giessen, "Cavity-enhanced localized plasmon resonance sensing," *Applied Physics Letters*, vol. 97, no. 25, pp. 2010–2013, 2010.

[42] Y. W. Fen and W. M. M. Yunus, "Characterization of the Optical Properties of Heavy Metal Ions Using Surface Plasmon Resonance Technique," *Optics and Photonics Journal*, vol. 01, no. 03, pp. 116–123, 2011.

[43] N. H. Zainuddin, Y. W. Fen, A. A. Alwahib, M. H. Yaacob, N. Bidin, N. A. S. Omar, and M. A. Mahdi, "Detection of adulterated honey by surface plasmon resonance optical sensor," *Optik*, vol. 168, no. 2010, pp. 134–139, 2018. [Online]. Available: https://doi.org/10.1016/j.ijleo.2018.04.048

[44] A. Hardy and W. Streifer, "Coupled Mode Theory of Parallel Waveguides," *Journal of Lightwave Technology*, vol. 3, no. 5, pp. 1135–1146, 1985.

[45] Y. Chen, "Nanofabrication by electron beam lithography and its applications: A review," *Microelectronic Engineering*, vol. 135, pp. 57–72, 2015. [Online]. Available: http://dx.doi.org/10.1016/j.mee.2015.02.042

[46] S. W. Ahn, K. D. Lee, J. S. Kim, S. H. Kim, J. D. Park, S. H. Lee, and P. W. Yoon, "Fabrication of a 50 nm half-pitch wire grid polarizer using nanoimprint lithography," *Nanotechnology*, vol. 16, no. 9, pp. 1874–1877, 2005.

[47] S. Zou, F. Wang, R. Liang, L. Xiao, and M. Hu, "A nanoscale refractive index sensor based on asymmetric plasmonic waveguide with a ring resonator: A review," *IEEE Sensors Journal*, vol. 15, no. 2, pp. 646–650, 2014.

[48] X. Yi, J. Tian, and R. Yang, "Tunable Fano resonance in plasmonic MDM waveguide with a square type split-ring resonator," *Optik*, vol. 171, pp. 139–148, 2018. [Online]. Available: https://doi.org/10.1016/j.ijleo.2018.06.027